RESEARCH ARTICLE

Key Points:
- Obtained remarkably consistent CH_2O scavenging efficiencies of 41 to 58% in all but one storm
- Six of seven different methods produced the same result on one storm within a 7% range
- Erroneous scavenging efficiencies result when inflow and outflow are not coherently related

Correspondence to:
A. Fried,
Alan.Fried@colorado.edu

Convective transport of formaldehyde to the upper troposphere and lower stratosphere and associated scavenging in thunderstorms over the central United States during the 2012 DC3 study

A. Fried[1], M.C. Barth[2], M. Bela[3], P. Weibring[1], D. Richter[1], J. Walega[1], Y. Li[4], K. Pickering[5], E. Apel[2], R. Hornbrook[2], A. Hills[2], D. D. Riemer[6], N. Blake[7], D.R. Blake[7], J. R. Schroeder[7], Z. J. Luo[8], J. H. Crawford[9], J. Olson[9], S. Rutledge[10], D. Betten[11], M. I. Biggerstaff[11], G.S. Diskin[9], G. Sachse[9], T. Campos[2], F. Flocke[2], A. Weinheimer[2], C. Cantrell[3], I. Pollack[10], J. Peischl[12,13], K. Froyd[12,13], A. Wisthaler[14,15], T. Mikoviny[15,16], and S. Woods[17]

[1]Institute of Arctic and Alpine Research, University of Colorado Boulder, Boulder, Colorado, USA, [2]National Center for Atmospheric Research, Boulder, Colorado, USA, [3]Atmospheric and Oceanic Sciences, University of Colorado Boulder, Boulder, Colorado, USA, [4]Department of Atmospheric and Oceanic Science, University of Maryland, College Park, Maryland, USA, [5]NASA Goddard Space Flight Center, Greenbelt, Maryland, USA, [6]Rosenstiel School of Marine & Atmospheric Science, University of Miami, Miami, Florida, USA, [7]Department of Chemistry, University of California, Irvine, CaliforniaUSA, [8]City College of New York, CUNY, New York, New York, USA, [9]NASA Langley Research Center, Hampton, Virginia, USA, [10]Department of Atmospheric Science, Colorado State University, Fort Collins, Colorado, USA, [11]School of Meteorology National Weather Center, University of Oklahoma, Norman, Oklahoma, USA, [12]NOAA/ESRL, Boulder, Colorado, USA, [13]CIRES, University of Colorado Boulder, Boulder, Colorado, USA, [14]Institute of Ion Physics and Applied Physics, University of Innsbruck, Innsbruck, Austria, [15]Department of Chemistry, University of Oslo, Oslo, Norway, [16]Oak Ridge Associated Universities, Oak Ridge, Tennessee, USA, [17]SPEC Inc., Boulder, Colorado, USA

Abstract We have developed semi-independent methods for determining CH_2O scavenging efficiencies (SEs) during strong midlatitude convection over the western, south-central Great Plains, and southeastern regions of the United States during the 2012 Deep Convective Clouds and Chemistry (DC3) Study. The Weather Research and Forecasting model coupled with chemistry (WRF-Chem) was employed to simulate one DC3 case to provide an independent approach of estimating SEs and the opportunity to study CH_2O retention in ice when liquid drops freeze. Measurements of CH_2O in storm inflow and outflow were acquired on board the NASA DC-8 and the NSF/National Center for Atmospheric Research Gulfstream V (GV) aircraft employing cross-calibrated infrared absorption spectrometers. This study also relied heavily on the nonreactive tracers *i-/n*-butane and *i-/n*-pentane measured on both aircraft in determining lateral entrainment rates during convection as well as their ratios to ensure that inflow and outflow air masses did not have different origins. Of the five storm cases studied, the various tracer measurements showed that the inflow and outflow from four storms were coherently related. The combined average of the various approaches from these storms yield remarkably consistent CH_2O scavenging efficiency percentages of: 54% ± 3% for 29 May; 54% ± 6% for 6 June; 58% ± 13% for 11 June; and 41 ± 4% for 22 June. The WRF-Chem SE result of 53% for 29 May was achieved only when assuming complete CH_2O degassing from ice. Further analysis indicated that proper selection of corresponding inflow and outflow time segments is more important than the particular mixing model employed.

1. Introduction

Ozone (O_3) is one of the key gases of interest in atmospheric studies, as it plays multiple roles in the atmosphere. Ozone trends affect the Earth's radiation budget, the flux of ultraviolet radiation to the surface, and the production of radical species that are responsible for the removal of primary pollutants. In the lower stratosphere (LS), catalytic chemical cycles involving radical species (hydrogen oxide radicals and/or various halogen species, such as chlorine and bromine oxides) result in net ozone destruction. In the upper troposphere (UT), chemistry-involving HO_x ($= OH + HO_2$) and NO_x ($= NO + NO_2$) radicals in the presence of volatile organic compounds (VOCs) results in net ozone production. It can be shown that net O_3 production in the UT/LS can be approximated by the following difference between production (P) and loss (L) terms [*Jaeglé et al.*, 1998, and references therein]:

$$P(O_3)-L(O_3) = k_1[NO][HO_2]-\left\{ k_4\left[O\left({}^1D\right)\right][H_2O] + k_6[HO_2][O_3] + k_5[OH][O_3]\right\} \tag{1}$$

The first term on the right, the reaction between NO and HO_2, accounts for approximately 80% of O_3 production in the UT [*Müller and Brasseur*, 1999]. An additional 5–15% is produced by the reaction between NO and CH_3O_2 radicals. It is clear that net O_3 production in the UT/LS is highly dependent upon HO_x, NO_x, as well as the concentrations of peroxides (hydrogen peroxide, H_2O_2, and methyl hydroperoxide, CH_3OOH) and oxygenated volatile organic hydrocarbons (OVOCs), which generate HO_2 and CH_3O_2 radicals when photolyzed. Oxygenated volatile organic hydrocarbons such as acetone, ethanol, methanol, formaldehyde (CH_2O), and acetaldehyde, to name a few, are important in this regard. The photolysis of CH_2O can be particularly important since its radical photolysis channel can rival other sources of HO_x radicals in the UT/LS where HO_x production from $O\left({}^1D\right)$ with water decreases as the available water vapor decreases with altitude [*Wennberg et al.*, 1998]. Hence, in order to better understand O_3 in the UT/LS, one needs to further understand the dynamical and chemical processes that control the concentrations of these OVOCs in this region. Deep convection is one means by which OVOCs from the boundary layer (BL) can be efficiently transported to the UT/LS [e.g., *Chatfield and Crutzen*, 1984; *Dickerson et al.*, 1987; *Pickering et al.*, 1990; *Jaeglé et al.*, 1997; *Brunner et al.*, 1998; *Crawford et al.*, 2000; *Dye et al.*, 2000; *Huntrieser et al.*, 2002; *Ridley et al.*, 2004a, 2004b; *Cooper et al.*, 2006; *Bertram et al.*, 2007; *Ancellet et al.*, 2009; *Barret et al.*, 2010; *Avery et al.*, 2010; *Barth et al.*, 2012]. Over the central United States, thunderstorms, which range in intensity from airmass to multicellular and supercells to mesoscale convective systems (MCS), occur on a near daily basis during the late spring and summer [e.g., *Carbone et al.*, 2002]. Hence, in addition to deep convection in the tropics, continental thunderstorm convection can play an important role in affecting O_3 concentrations in the UT/LS.

While nonsoluble trace gases with chemical lifetimes longer than convective transport times (10–60 min) will be lofted in convection, transport of soluble trace gases like CH_2O is less certain. Formaldehyde with its moderately high Henry's law constant of 3.2×10^3 M atm^{-1} at 298 K [*Sander*, 2015] is thought to be mostly removed during convection. Convective cloud modeling studies such as *Barth et al.* [2007] suggest that gas-phase CH_2O is largely depleted during deep convective storms due to uptake in liquid and ice hydrometeors. Assuming no reemission of CH_2O from the ice phase, which itself is a major unanswered question, *Barth et al.* [2007] calculate that 10%–15% of the boundary layer CH_2O in the gas phase makes it to 12 km in the simulation of deep convection on 10 July 1996 during the Stratospheric Tropospheric Exchange: Radiation, Aerosols and Ozone (STERAO) campaign. This campaign took place over northeastern Colorado. Furthermore, approximately two thirds of the background gas-phase CH_2O present at 10 km is removed after ~ 1 h of processing in this storm. The Barth study reveals that many factors involving microphysical processes (cloud hydrometeor type, pH, temperature, drop size, drop speed, liquid and ice water contents, liquid phase chemistry, and the residence time the species is in contact with the liquid phase) are involved in properly assessing CH_2O transport and uptake efficiencies during deep convective transport to the UT/LS, and hence, this study indicates that high-accuracy CH_2O measurements are needed to help in validating these models for such moderately soluble species. Even when such measurements were available during anvil penetrations for another STERAO storm, the 3-D cloud scale chemical transport model results of *DeCaria et al.* [2005], which did not include CH_2O in the ice phase, were still ~ a factor of 2 low compared to CH_2O measurements by the Fried group acquired on the NOAA WP3 aircraft during the 12 July 1996 STERAO storm. Thus, major uncertainties still exist regarding the behavior of soluble O_3 and radical precursors such as CH_2O during convection. The two more recent papers by Fried and colleagues [*Fried et al.*, 2008a, 2008b] during the NASA INTEX-NA campaign in 2004 over the continental United States and the North Atlantic Ocean provided further evidence regarding enhancements in CH_2O in the UT/LS during continental convection. In the altitude range between 6 and 12 km, *Fried et al.* [2008b] found that ~40% of the CH_2O observations and model values were perturbed above background values (upper limit, 165 parts per trillion by volume (pptv)) by as much as 1.5 parts per billion by volume (ppbv) due to such convection.

A number of studies have documented enhancements in CH_2O in the UT impacted by convection in different regions of the world, including the tropical Pacific region during the PEM-Tropics B study [*Raper et al.*, 2001; *Mari et al.*, 2003; *Pickering et al.*, 2001], the Mediterranean basin during MINOS [*Lelieveld et al.*, 2002; *Kormann et al.*, 2003], central Europe during UTOPIHAN [*Colomb et al.*, 2006; *Stickler et al.*, 2006], North America and the North Atlantic region during INTEX-NA [*Fried et al.*, 2008a, 2008b], and the West African region during the 2006 AMMA study [*Borbon et al.*, 2012]. The last study provided estimates of CH_2O scavenging efficiencies (SEs) for four MCS case studies. This parameter, which is critical for determining the relative contributions of the various HO_x precursors, is calculated from equation (2).

$$SE = \frac{\left\{ [CH_2O]_{Anvil\ core\ calc.} - [CH_2O]_{OF\ measured} \right\}}{[CH_2O]_{Anvil\ core\ calc.}} \tag{2}$$

In this equation $[CH_2O]_{Anvil\ core\ calc.}$ represents the CH_2O concentration ingested into the convective cloud that ultimately exits the top of the convective core. This term, which is based upon the measured storm inflow (IF) concentrations, takes into account dilution by lateral entrainment of background air. The term $[CH_2O]_{OF\ measured}$ is the CH_2O concentration measured in the anvil outflow (OF). The determination of these parameters will be further discussed in a later section.

Barth et al. [2007] discuss a number of methods employed in past studies in determining trace gas scavenging efficiencies, which includes the studies by *Giorgi and Chameides* [1986] and *Easter and Hales* [1983]. *Cohan et al.* [1999] devised a two-component mixture model: an insoluble trace gas X measured near convective outflow (X_{conv}) is expressed as a mixture of air transported from the boundary layer (BL) and air from the nearby upper troposphere (UT) such that: $X_{conv} = \beta X_{BL} + (1 - \beta)X_{UT}$, where β measures the fractional contribution from the BL. The fraction β can be evaluated based upon aircraft measurements of X_{conv}, X_{UT}, and X_{BL}. For a soluble gas Y, the equation is written as $Y_{conv} = (1 - SE)\beta Y_{BL} + (1 - \beta)Y_{UT}$, where SE is the scavenging efficiency by convective clouds. While this two-component mixture model gave reasonable results in the *Cohan et al.* [1999] study, it did not consider lateral entrainment of free tropospheric air into the convective core as air was lofted upward. *Borbon et al.* [2012] proposed a three-component mixture model to deal with lateral entrainment from midlevel free tropospheric air. In this model, X_{conv} is expressed as a mixture of three components: $X_{conv} = \beta X_{BL} + \alpha X_{FT} + (1 - \alpha - \beta)X_{UT}$, where X_{FT} represents the contribution from the free troposphere and α is the bulk entrainment rate. A third variable, the detrainment fraction δ (where $\delta = \beta + \alpha$), was introduced and three insoluble tracers, benzene, toluene, and CO, were used in solving three equations with three unknowns. The equation for a soluble gas is modified accordingly as $Y_{conv} = (1-SE)(\beta X_{BL} + \alpha X_{FT}) + (1-\alpha-\beta)X_{UT}$. *Borbon et al.* [2012] applied this model to mesoscale convective systems (MCSs) observed in West Africa. The MCSs are known to ingest air from a deep layer, including air above the BL [*Houze*, 1993]. Although this approach is an improvement in simulating MCS storms, the sampling constraints discussed by *Borbon et al.* [2012] place limitations on the analysis. This approach (1) relies on one value for X_{FT} (2–8 km region), which represents a mixing ratio in a region where layers of different types of air and therefore different mixing ratios could reside, (2) assumes that the β term properly accounts for dilution/mixing when trace gases emanate from the top of the convective core to the time of sampling in the anvil outflow, and (3) assumes constant values for the three parameters over different storms, and thus as pointed out by *Borbon et al.* [2012], does not take into account variability of entrainment, mixing, and detrainment processes. In addition, we have found on occasion that small differences between convectively enhanced tracer concentrations (X_{conv}) like CO and its nontrivial background upper troposphere (X_{UT}) values can result in large uncertainties in the three retrieved parameters (α, β, and δ), which on some occasions yield unrealistic values. This will be discussed further.

The various studies mentioned above report a rather large range for CH_2O SEs. For example, *Barth et al.* [2007] calculate CH_2O SEs ranging between 11% and 57% for the 10 July 1996 STERAO simulations. The large range reflects different assumptions in the calculations, where the lowest SE reflects reemission of CH_2O from the ice phase back into the gas phase. Earlier simulations by *Pickering et al.* [2001] for convection over the South Pacific during PEM-Tropics B report a CH_2O SE of 78%. Likewise, *Borbon et al.* [2012] report a large SE range of 4% to 39% for four MCS storms based upon measurements during the AMMA study. Because of its significance, it is important to further investigate the various factors involved in controlling CH_2O SEs.

The focus of the present study is to reinvestigate CH_2O SEs in a variety of thunderstorm types employing different analysis approaches and extensive measurements acquired from two different aircraft platforms, the NASA DC-8 and the NSF/NCAR Gulfstream V (GV), during the Deep Convective Clouds and Chemistry (DC3) Study in 2012 [*Barth et al.*, 2015]. The DC3 study was conducted between 10 May and 30 June 2012 out of Salina, Kansas, sampling storms in and around Oklahoma, North Texas, Colorado, and Alabama. Five storm cases were studied. The two aircraft in the present study flew in close coordination to sample convective inflow and outflow in near-simultaneous fashion. Most of the boundary layer inflow measurements were acquired by the NASA DC-8 aircraft while both the DC-8 and GV provided anvil outflow measurements. Occasionally, the aircraft switched roles. Ground-based radar networks, LMAs, and weather balloons obtained data on storm kinematics and structure, lightning, and the storm thermodynamic environment. In addition to intercompared measurements of CH_2O, both aircraft deployed extensive measurements of various nitrogen

oxide species, peroxides, CO, water vapor, CH_4, organic tracers, and VOCs and OVOCs (see *Barth et al.* [2015] for a complete list of species measured on both aircraft). To our knowledge, the DC3 study employed one of the most comprehensive, if not the most comprehensive, payloads for convective studies. Such comprehensive payloads allowed us to further establish that storm outflow measurements were coherently related to storm inflow measurements (i.e., the outflow was not significantly perturbed by air parcels from locations other than the BL inflow regimes considered) in four of the five cases studied. The importance of establishing this coherence cannot be overstated when quantifying SEs. As we will show, in the one example where this was not the case we obtained high (>80%) CH_2O SEs.

The analysis in one DC3 case analyzed here (29 May storm) is supported by a cloud-resolving chemistry transport model (a high-resolution Weather Research and Forecasting model coupled with Chemistry, WRF-Chem). By conducting sensitivity simulations with the WRF-Chem model, where we compare CH_2O SEs determined by two approaches (to be discussed) with those derived from WRF-Chem assuming different amounts of CH_2O retained in the ice, allows us to further investigate the role of ice in scavenging CH_2O.

The five storms studied here represent different storm characteristics and different boundary layer inflow compositions. As will be discussed in section 4, CH_2O SEs are determined for each storm employing two different approaches, an altitude-dependent entrainment model and a butane ratio method, in addition to the WRF-Chem analysis for the 29 May storm. In section 6, we also present results for the 29 May storm employing the *Borbon et al.* [2012] three-component mixture model as well as the *Cohan et al.* [1999] two-component mixture model to investigate differences between models employing the same data set. This provides further insights into factors that might affect CH_2O SE determinations.

2. Airborne CH_2O Measurements

The present study was based on CH_2O measurements primarily acquired from two similar infrared absorption spectrometers employing difference frequency generation (DFG) laser sources: the DFGAS (Difference Frequency Generation Absorption Spectrometer) instrument on the NASA DC-8 [*Weibring et al.*, 2006, 2007] and the newer more sensitive CAMS (Compact Atmospheric Multispecies Spectrometer) instrument [*Richter et al.*, 2015] on the NSF/NCAR GV aircraft. The CAMS instrument provided CH_2O data with 1–2 s time resolution and with estimated accuracy and limits of detection (LODs at 1σ) of around 4% and 15–30 parts-per-trillion by volume (pptv), respectively. The LODs marginally improved to 15–20 pptv when using 1 min averages. The DFGAS instrument provided data with similar time resolution and estimated accuracy but with 1 s LODs in the 47 to 66 pptv range, with most values falling in the 50–60 pptv range. The 1 min LOD improved to around 20 pptv. Both data sets can be found in the NASA Langley data archive at http://www-air.larc.nasa.gov/missions/dc3-seac4rs/index.html. As will be discussed, the radar storm images employed here are displayed in 10 min blocks, and therefore in this study, we employ the 1 s CH_2O data from both instruments averaged to 1 min. The header information from both data sets provides extensive information on the measurement techniques and how these LODs and accuracy estimates were determined. Data from these two instruments were employed throughout the present data analysis with the exception of GV data acquired on 11 June 2012. In this case, a laser drive connector failed on the CAMS instrument and the analysis involving GV outflow relied on CH_2O measurements acquired by the TOGA (Trace Organic Gas Analyzer) instrument [*Apel et al.*, 2014, and references therein]. This instrument provided a 35 s integrated measurement every 2 min with a CH_2O uncertainty of ± 50% or 200 pptv (whichever is greater) and an LOD of 20 pptv.

2.1. CAMS and DFGAS CH_2O Instruments

The core design, sampling, data acquisition, zeroing, and calibration of the DFGAS and CAMS instruments are similar. As both instruments have been discussed in detail elsewhere, we only provide an overview here. In both instruments, ambient air is sampled through heated (35°C) forward facing electropolished stainless steel (1/2 inch OD tubing) HIMIL (HIAPER Modular Inlet) inlets. These inlets have restrictions on the outlets to provide a small RAM-air boost for sampling at high altitudes and high aircraft speeds (~60 torr boost at ~206 m/s above ~10 km). Large particles greater than ~1 μm (estimate) are excluded by subsampling near the center of the HIMIL at right angles through ~41 cm of heated 0.5 inch electropolished stainless tubing, which in turn is connected to several feet of 0.5 inch heated PFA Teflon line. The exact length depends on the particular aircraft platform. A 0.25 inch side arm is connected to the sampling arm of both inlets at ~10 cm downstream of the right

angle junction for introduction of CH_2O calibration standards and zero air (air devoid of CH_2O) in flight (to be discussed). In both cases, the sampled air is then directed through MKS T3B pressure controlling throttle valves, which have very low pressure drops of ~1 torr at flow rates of 10 slm (in all cases, standard conditions refer to 1 atmosphere pressure and 273 K). This valve in conjunction with the RAM-air pressure boost is necessary for sampling at high altitudes and high speeds. Laboratory tests have been carried out to ensure 100% CH_2O transmission through the inlet systems. The controlling valves are set to maintain sampling pressures of 50 torr through the sampling cells in both instruments. In CAMS, the sampled air is directed through a nonastigmatic multipass Herriott absorption cell (89.6 m pathlength in ~1.5 L volume) using flow rates in the 4–5-slm range (cell residence time ~1.2–1.5 s). The DFGAS instrument employs a 100 m pathlength astigmatic multipass cell (4.3 L volume) using flow rates in the 8.5–9.5-slm range (cell residence time ~1.6–1.8 s).

Both instruments rely on absorption of midinfrared laser light at a moderately strong CH_2O absorption feature at 3.53 μm (2831.6 cm^{-1}) employing DFG laser sources. This feature is free of all known spectroscopic interferences with the exception of weak methanol features (to be further discussed). Light at 3.53 μm is generated by mixing two near-IR room temperature lasers (one at 1562 nm and the other at 1083 nm) in a nonlinear crystal (periodically poled lithium niobate) via difference frequency generation (DFG). The transmitted light from the sampling cells is detected by photovoltaic mercury cadmium telluride detectors.

Both instruments rely on frequent background measurements (after every 60 s ambient sample cycle) by introducing zero air to the inlet employing onboard CH_2O scrubbing units. This frequent zeroing procedure very effectively captures and removes optical noise, residual outgassing from inlet line and cell contaminants, and continuously purges the sampling surfaces to minimize the buildup of organic contaminants that could react with O_3 to produce artifact CH_2O. Evidence for the absence of the latter issue will be shown in a later section. These precautions are important to ensure high measurement accuracy, particularly when sampling UT/LS outflow following much higher concentration boundary layer measurements. Retrieved CH_2O mixing ratios are determined in 1 s increments by fitting acquired ambient spectra to reference spectra, obtained by introducing high-concentration calibration standards from onboard permeation calibration systems whose absolute mixing ratios are determined using the fundamental approach of direct absorption employing the Beer-Lambert relationship and fundamental spectroscopic parameters (line position, absorption coefficient, and broadening parameters). Thus, the two instruments are tied to a common absolute reference (see the header information in both data sets for more information). Periodically, calibration standards are introduced during flight in both instruments (on top of zero air and ambient air) to ensure calibration stability and sampling line/cell transmission efficiency. *Apel et al*. [2014] provide a discussion of the TOGA instrument.

2.2. DFGAS-CAMS-TOGA Comparison Regressions

One of the strengths of the DC3 study is that instruments measuring the same constituents on the NASA DC-8 and NSF/NCAR GV aircraft were intercompared on five different flights during wingtip comparisons to ensure that storm inflow-outflow comparisons were not influenced by instrument biases. In this paper we focus only on comparisons of trace gases employed in the analysis here (CH_2O, *i-/n*-butanes, *i-/n*-pentanes). Figure 1 shows the 1 s DFGAS measurements on the DC-8 averaged over the CAMS time base (*Y* axis) as a function of the 1 s CAMS measurements (*X* axis) for wingtip comparisons carried out on 25 May, 30 May, 1 June, 5 June, and 17 June 2012. Nearly identical regression fits are obtained using either the 1 s or the data averaged in 100 pptv bins. As can be seen, the DFGAS instrument yields CH_2O values 13.5% higher than the CAMS instrument, despite the fact that the two instruments are tied to a common absolute reference standard and employ similar zero air scrubbing systems. However, wingtip comparisons of the two instruments during the 2014 FRAPPÉ (Front Range Air Pollution and Photochemistry) Study using careful postmission laboratory methanol standard additions revealed agreement to within 0.6% in the 1–1.5 ppbv CH_2O concentration range and 4.8% in the 200–400 pptv range. The CAMS instrument was found to be 2.4 times more sensitive to methanol as DFGAS for a number of reasons. During the DC3 study, the two instruments employed different methods to remove the methanol interference. In DFGAS, the methanol interference was removed by subtracting the methanol contribution (1.2% times the methanol concentration, which has been determined from extensive laboratory measurements) using methanol measurements from the PTRMS instrument on the DC-8 interpolated to the DFGAS time base. Comprehensive details regarding the PTRMS instrument and associated data can be found on the NASA Langley data archive (http://www-air.larc.nasa.gov/missions/dc3-seac4rs/index.html) under the PI Directory name Wisthaler.Armin. By contrast, CAMS removed this interference using a postmission
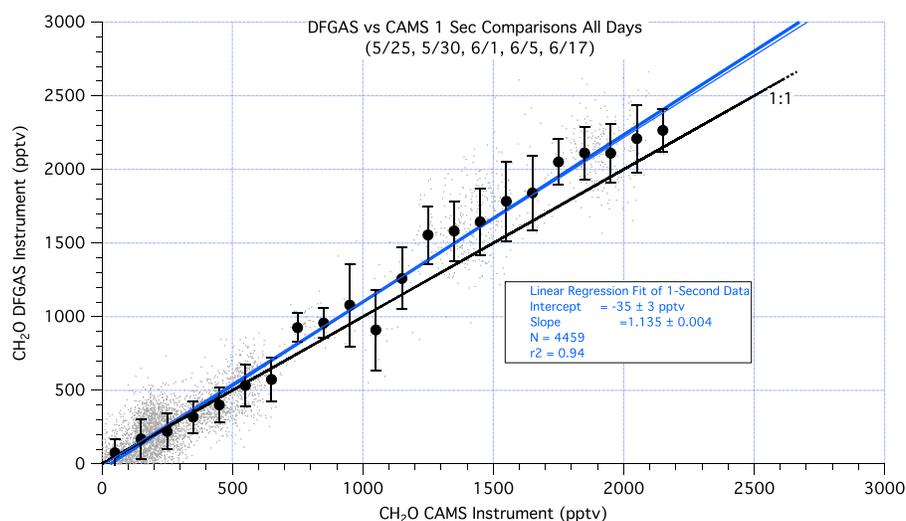
Figure 1. The 1 s DFAS CH_2O concentrations averaged over CAMS time base as a function of 1 s CAMS measurements acquired during wingtip comparisons on five different days (light gray points) and the linear regression fit of these data (dark blue line, whose statistics are given in the box). The nearly identical light blue regression line is a linear fit of the binned DFGAS averages (100 pptv bins) depicted by the dark circles and the 1 standard deviation bars (intercept = -10 ± 39 pptv, slope = 1.113 ± 0.032, $r^2 = 0.98$, N = 23).

laboratory-generated model in which the methanol features were fitted simultaneously with CH_2O. Although the latter method is preferred, the CAMS corrections were confounded by the fact that methanol was to some extent also transmitted by the zero air scrubber in CAMS due to a contamination in CAMS but not in DFGAS. For these reasons our original 4% CAMS uncertainty estimate needs to be increased by perhaps as much as 10% during the DC3 Study (subsequent studies employing CAMS do not have this complication). Despite these differences, the CAMS corrected outflow data (corrected by the regression slope and intercept given in Figure 1, inset box) only differ by 100 to 150 pptv from the uncorrected data over the range of CH_2O concentrations encountered. Likewise, the TOGA CH_2O measurements on the GV for the 11 June study were corrected to DFGAS by linear regression of the wingtip comparison data. For this case, the 1 s DFGAS measurements were averaged over the 35 s TOGA start and stop times to generate a data set (N = 53 points) for comparison. The linear regression (not shown) fit yields the following:

$$DFGAS_{fit} = -(54\pm32) \text{ pptv} + (0.96\pm0.031)\times TOGA, \ r^2 = 0.95 \qquad (3)$$

These corrections ensure consistency among the three CH_2O measurements.

In the case of the primary tracers employed (to be discussed) n-butane, i-butane, n-pentane, and i-pentane, the corresponding TOGA accuracy and LODs are $\pm 15\%$ or 2 pptv (whichever is greater) and 1 pptv, respectively. The corresponding values for the Whole Air Sampler (WAS) on the DC-8 are 5% accuracy and 3 pptv LOD. Comparisons of final butane and pentane data acquired by TOGA versus WAS during the five intercomparison flights required us to first expand out both data sets to 1 s time intervals to match up time-coincident periods for both of the relatively slow hydrocarbon instruments (35 s for TOGA and ~ 0.5 min to > 2 min for WAS, depending upon altitude). This resulted in linear regression slopes (TOGA, Y axis versus WAS, X axis) of: 0.90 (n-butane), 0.86 (i-butane), 0.94 (n-pentane), and 0.81 (i-pentane) with small intercepts all less than 7 pptv. Table 1 further tabulates time-coincident (TOGA-WAS) differences for the five wingtip comparison flights. The number of distinct comparisons is significantly less than the apparent number of comparisons produced by the time expansion process, which generates multiple identical values. The distinct number of comparisons is given in this table by N in the last column. Comparisons of the i-/n-butane and pentane ratios, also given in Table 1, will be used in a subsequent discussion.

3. Overview of DC3 CH_2O Measurements

Figure 2 depicts the flight tracks for the DC-8 and GV aircraft over the course of the DC3 study from 18 May to 22 June 2012 [*Barth et al.*, 2015] when both aircraft were in operation. These flight tracks cover a large portion

Table 1. Time-Coincident VOC Wingtip Comparisons[a]

| Measurement	(TOGA-WAS)			
	Average	Standard Deviation	Median	N
n-butane	−41	71	−6	60
i-butane	−26	40	−5	50
i/n-butane	−0.032	0.14	−0.006	49
n-pentane	−7	15	−3	45
i-pentane	−22	39	−9	46
i/n-pentane	0.012	0.35	−0.068	45

[a]The average, standard deviation, and median (TOGA-WAS) point-by-point comparisons are shown. All concentration measurements are in pptv units, while the i-/n-butane and pentane ratios have no units. The number N represents the number of distinct comparisons (see text).

of the central and eastern United States. Figure 3 shows an overview of the CH_2O data acquired by both instruments during these flight tracks as a function of altitude. The CAMS data were not corrected here by the wingtip comparisons nor are the data aligned for time coincidence or geographic coincidence. The 22 June data, which in many cases are influenced by the High Park fire plume over Colorado, are highlighted by darker points. For reference, the 6–12 km background range (0 to 165 pptv) determined by *Fried et al.* [2008b] from INTEX-NA is denoted by the black rectangles. As can be seen in the figure by the C-shape profiles, enhanced CH_2O levels as high as 1800 pptv occur at altitudes up to 12.5 km arising from deep convective transport. The fire-influenced data of 22 June, which show even higher CH_2O enhancements in the 5000–6000 pptv range, will be discussed in a later section. These observed enhancements suggest that a significant fraction of CH_2O is transported from the boundary layer to the upper troposphere, providing mixing ratios in convective outflow regions that are much greater than the UT background. This suggests that CH_2O is an important precursor to HO_x and O_3 production in these outflow regions as they are transported in the UT.

4. CH_2O SE Determinations During the DC3 Campaign

This section provides an overview of the two analysis approaches (altitude-dependent entrainment model and butane ratio method) employed in the determination of CH_2O SEs for the five storms cases studied as well as a third method (cloud-resolving chemistry transport model employing WRF-Chem) for the 29 May storm. The five storms studied represent different storm characteristics and different boundary layer inflow compositions. The storms, whose locations are shown in Figure 4, are the following: (1) the 29 May storm over central Oklahoma; (2) the 6 June storm over northeast Colorado; (3) the 11 June storm over Arkansas, Missouri, Illinois, and Mississippi; (4) the 21 May storm over northern Alabama and Tennessee; and (5) the 22 June storm over Colorado and Nebraska, which was influenced by the High Park fire. Table 2 gives the characteristics of these storms. The latter two storms, which are highlighted by shaded color in Figure 4, are included in this study to underscore the importance of identifying potential confounding factors that can influence SE determinations.
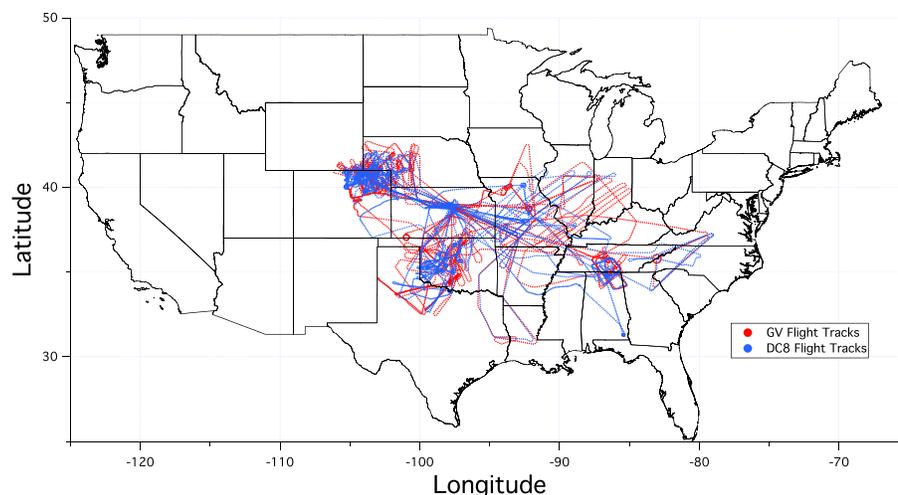

Figure 2. DC-8 and GV flight tracks from 1 min merged data, 18 May through 22 June 2012.
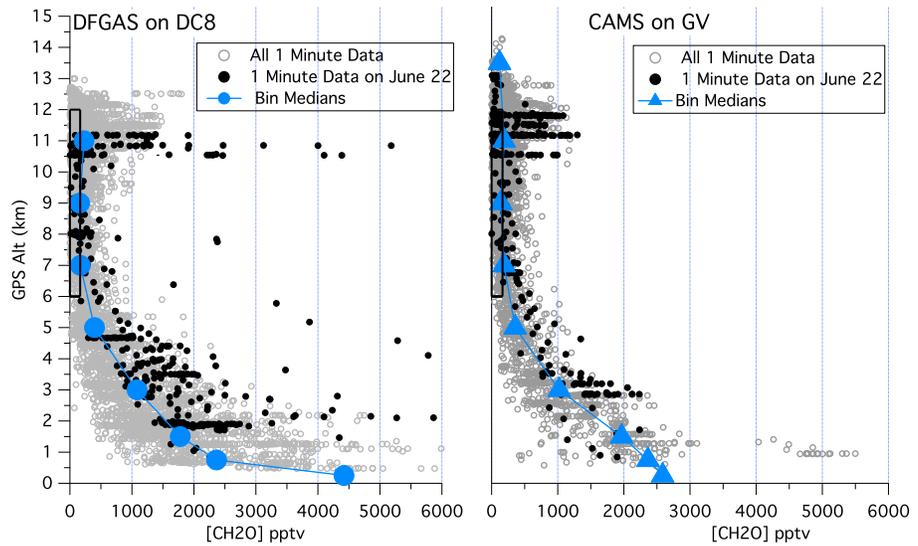
Figure 3. One minute merged CH$_2$O data and binned medians for the DFGAS and CAMS instruments (not corrected by the regression of Figure 1) during DC3 from 18 May to 22 June 2012 plotted versus GPS altitudes. Convectively enhanced CH$_2$O is clearly evident in the UT/LS in both data sets by the C-shape profiles, which are neither time-coincident nor coaligned geographically here. For reference, the 6–12 km background CH$_2$O range (0 to 165 pptv) determined by *Fried et al.* [2008b] during INTEX-NA is denoted by the black rectangles. The 22 June data, which in many cases are influenced by the High Park fire plume over Colorado, are highlighted by darker points. These points are not included in the Bin Medians.

4.1. Convective Tracers Employed in This Study

The ideal tracer of convective transport should exhibit the following properties: (1) low reactivity over convective transport time scales (less than ~ 20 min for the storms studied here, as will be further discussed), (2) low solubility, (3) elevated and uniform BL concentrations from the source regions under study, (4) directly originating from the BL and not produced by secondary chemistry from other species, and (5) large convectively enhanced concentrations in the UT/LS that are clearly distinguishable from low nonconvectively perturbed background values. In addition, it is desirable to further select tracer pairs with similar OH reaction rate constants to identify air masses that have been impacted by other source regions.
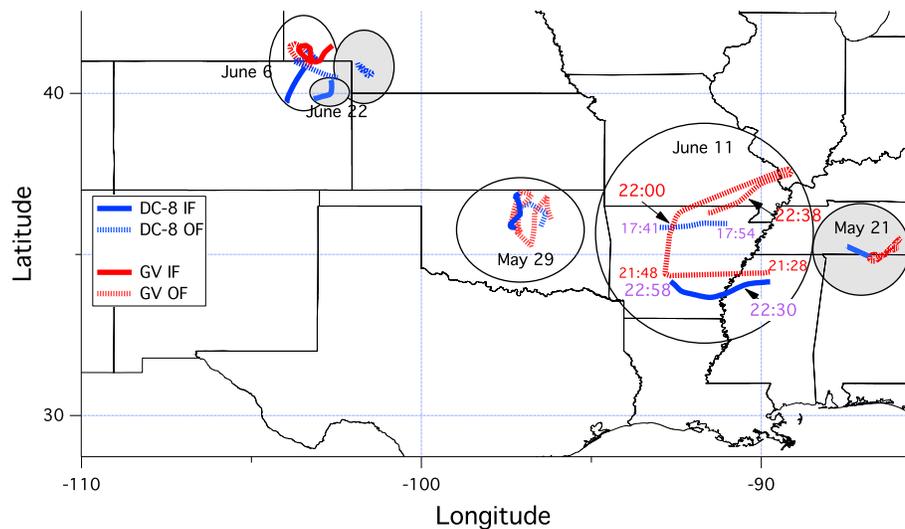
Figure 4. Three primary sampling regions (29 May, 11 June, and 6 June) and two additional regions (22 June and 21 May highlighted by shaded color) further examined in this study, depicting DC-8 inflow (IF) and outflow (OF) locations along with GV inflow (IF) and outflow (OF) locations. The two shaded additional regions, which were also included in this study, highlight the importance of identifying potential confounding factors that can plague SE determinations (see text for further discussion).

Table 2. Storm Cases Studied[a]

| Date/Region	Maximum Vertical Velocity	Type of Convection	Maximum IWC in OF
21 May/Alabama	20	Weak air mass thunderstorm	NA
29 May/Oklahoma	45–60	Severe multicell storm with common anvil	1.24
6 June/Colorado	35	Severe storm	0.22
11 June/Arkansas	No dual Doppler radar coverage	Severe MCS	1.7
22 June/Colorado	No dual Doppler radar coverage	Isolated supercells, High Park Fire influenced	0.87

[a]The second column lists the maximum vertical velocity in m/s while the last column lists the ice water content (g/m^3) from the SPEC wing probe instrument on the DC-8 (this was not available, NA, for 21 May) and from the 2 DC Probe on the GV for 11 June.

In this study we employ the following four tracers for each storm, *n*-butane, *i*-butane, *n*-pentane, and *i*-pentane. Figure 5 displays the altitude binned median profiles (1 km bins) for these four tracers for the 29 May storm measured on the DC-8. This plot also shows the profiles for CH_2O, CO, *n*-hexane, and *n*-heptane. The UT convective OF enhancements between 9 and 11 km are clearly evident in each profile, and with the exception of CO, the altitude profiles for each of these gases are very similar. As can be seen, *n*-hexane and *n*-heptane also show UT convective OF enhancements that are clearly distinguishable from their non-convectively perturbed background values and are thus included with our four-selected tracers for the 29 May storm. In other storm cases, the enhancements for these higher alkanes are significantly lower (typically < 20 pptv) and are not employed due to added noise. The profiles for these other storms are similar to those of Figure 5, only with lower concentrations in general. In the case of CO, the midaltitude background concentrations are still significant, in contrast to the above tracers. This in turn makes the determination of the lateral entrainment rate (α) that much more sensitive to its midaltitude background concentrations. In section 6, we further discuss calculated entrainment rates, their dependence on the tracer altitude profiles, and the resultant effects on determined CH_2O SEs. In the process we will discuss the desired tracer altitude profiles for different analysis approaches.
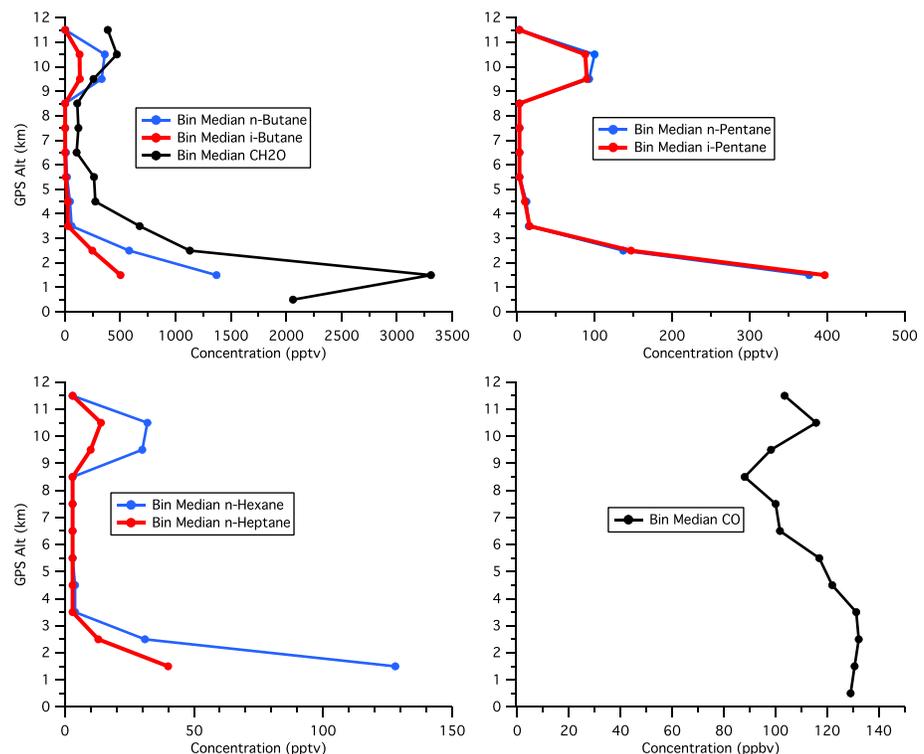
Figure 5. GPS altitude bin median concentrations (1 km bins) for the 29 May 2012 storm for various trace gases measured on the DC-8.
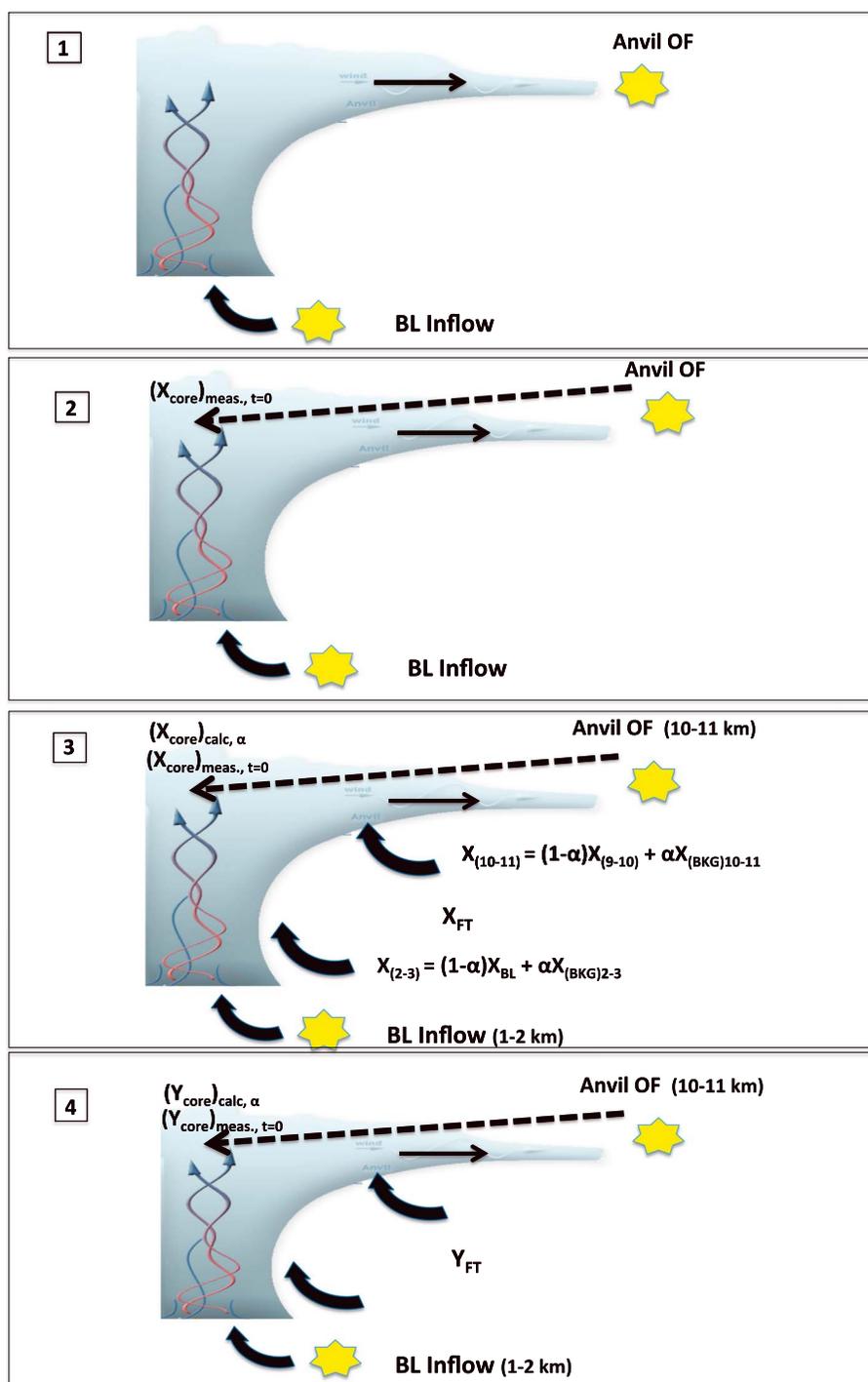
Figure 6. Conceptual altitude-dependent entrainment model showing the four steps employed. The stars represent the aircraft positions at the time of inflow (1–2 km shown here) and outflow sampling (10–11 km shown here). The organic tracers used in this analysis are represented by the notation **X** while CH_2O is represented by **Y**. See text for further details.

4.2. Altitude-Dependent Entrainment Model

This section gives an overview of the four steps we employ in the altitude-dependent entrainment model, and Figure 6 provides conceptual diagrams for this discussion. Section 4.5 provides more specific details using the 29 May storm case as an example. All SE determinations (even the WRF-Chem simulations) start with a careful analysis of the storm inflow (IF) and corresponding outflow (OF) time periods (Step 1 in Figure 6). These time

Table 3. Boundary Layer Inflow (IF) and Upper Troposphere Outflow (OF) Times[a]

Date	DC-8 IF Times	GV IF Times	DC-8 OF Times	DC-8 IF/OF Altitudes	GV OF Times	GV IF/OF Altitudes
21 May	19:30:43 to 19:38:00			1.23	20:50:30 to 21:14:30	10.4 ± 0
29 May	23:10:21 to 23:15:53	-	23:48:30 to 23:58:30	$1.3/10.9 \pm 0.2$	23:59:30 to 24:23:30	11.8 ± 0.1
6 June	22:13:40 to 22:25:12	23:50:30 to 23:55:30	23:56:30 to 24:09:30	$1.7/12.4 \pm 0.01$	22:20:30 to 22:53:30	$2.5/11.9 \pm 0.2$
11 June	22:29:30 to 22:57:30	-	-	$0.6 \pm 0.3/$	21:59:30 to 22:37:30	12.9 ± 0.3
22 June	22:31:27 to 22:45:54	-	25:16:30 to 25:20:30	$1.9/11.2 \pm 0.02$	-	-

[a]For the IF, 1 s resolved data are used in determining the tabulated times. For the OF, 1 s resolved time ranges are also given. However, since the aircraft-storm wind vectors that are used in the analysis (see text) and are given in 1 min intervals, all tabulated OF times are given on the 1 min merge sampling periods. Individual 1 min sampling periods within the tabulated ranges may not be included because they include stratospheric influence periods and/or periods with no outflow from the storm core under study (see the individual plots for the time periods included). The IF/OF altitudes were determined from the average GPS altitude (km) in the given time period.

periods are schematically indicated in this figure by stars. In the case of the 29 May storm, this step is particularly critical since, as will be shown, the boundary layer is very heterogeneous with respect to CH_2O and one of its important precursors isoprene. In this approach we superimpose both the DC-8 and GV aircraft positions with corresponding wind vectors on radar storm images (NWS NEXRAD images of maximum column reflectivity). The wind vectors depict the wind speeds and wind directions at the location of the aircraft. For inflow periods, we identify BL flight segments where the storm relative aircraft wind vectors (storm motion removed) indicates air flowing into the storm. For inflow measurements, removal of the storm motion is necessary since the storm speeds are generally much larger than the prevailing wind speeds at low altitudes. At high altitudes in the outflow the reverse is true and the storm motion is not removed.

Analogous to the inflow periods, the outflow periods are identified whenever the aircraft wind vectors point away from the storm cores toward the aircraft positions. In addition to enhancements of the various tracers and CH_2O, cloud indicators (SPEC particle concentration measurements on the DC-8 and RAF 2 DC particle concentration measurements on the GV) along with flight videos provide additional evidence when the aircraft are in clouds. In most cases, OF time periods are within ~ 1 h or less of the IF time periods, span the same geographic region, and correspond to the same storm core as the IF. This latter constraint is made more difficult by the evolving nature of the storm systems, with new core cells forming with time. Table 3 lists the inflow (IF) and upper tropospheric outflow (OF) time periods thus determined for the five storm cases studied here. In the case of the IF, the time ranges are resolved to the nearest second, and these ranges are consistent with those listed in *Barth et al.* [2016]. In the case of the OF, the time ranges are given on the 1 min merge sampling periods since the subsequent analysis employ the 1 min resolved wind vectors superimposed on the radar images. As a result, our OF time ranges encompass the ranges listed by *Barth et al.* [2016] but are slightly larger. Also, as will be discussed, individual 1 min sampling periods within the tabulated ranges may not be included because they include stratospheric influence periods and/or periods with no outflow from the storm core under study.

The second step in our altitude-dependent entrainment model (Step 2 in Figure 6) involves extrapolation of the measured organic tracers back to the storm core. For obvious safety reasons, the species concentrations at the storm core tops could not be determined by direct measurements in most cases, and thus, there was a finite amount of time from the top of the convective core to the time of aircraft sampling in the anvil outflow. To account for the resulting dilution/mixing and possibility of chemical transformations, we examine the outflow in each case employing the storm radar images, aircraft wind speeds, and directions along the flight tracks to graphically estimate the time between aircraft sampling and the closest intense storm core. In this procedure we measure the linear distance along the wind vectors between the aircraft and the storm core for comparable core intensities (radar reflectivities ≥ 40 dBZ). We employ these procedures since each of the outflow samples represent different outflow times, and this produces a time-dependent "apparent decay" due to mixing, dilution, photochemistry, as well as potential uptake within the anvil. This procedure allows us to empirically determine single tracer and CH_2O outflow-mixing ratios extrapolated to time 0 emanating from the storm core. These are, respectively, shown in Figures 6 (Step 2 and Step 4) as $(X_{core})_{meas., t=0}$ (tracer extrapolated to core) and $(Y_{core})_{meas., t=0}$ (CH_2O extrapolated to core). The application of this procedure to the 29 May storm case is further shown in Figure 9 (to be discussed). We note that this extrapolation yields mixing ratios at the storm core tops, whereas those tabulated by *Barth et al.* [2016] and *Bela et al.* [2016] employ average OF values, which produce midanvil OFs that are slightly lower than the extrapolated values here. This in turn would produce slightly higher CH_2O SEs than our extrapolated results.

We also eliminate in this analysis the extra complications caused by mixing in stratospheric air into the anvil outflow by eliminating measurements where O_3 levels are greater than 100 ppbv and CO levels are simultaneously less than 100 ppbv. These limits are slightly more stringent than those employed by *Barth et al.* [2016] and *Bela et al.* [2016], who use O_3/CO ratios > 1.25 to identify and eliminate stratospheric air. Such stratospherically influenced periods are immediately obvious in the GV periods shown in Figures 8b and 9 (to be shown and further discussed in a later Section). As can be seen, the CH_2O CAMS (not corrected to DFGAS here) measurements drop to values below 50 pptv as the O_3 levels exceed 200 ppbv, adding credence to our claim that our sampling strategy discriminates against the build up of organic contaminants which can react with O_3 to produce CH_2O on inlet surfaces. The DFGAS instrument on the DC-8 showed that similar behavior when O_3 measurements provided by T. Ryerson at NOAA and his group was elevated.

The third step in our analysis (Step 3, Figure 6) utilizes the various convective tracers discussed previously in determining the lateral entrainment rate (α). Following the entraining plume model commonly used in general circulation model cumulus parameterizations [e.g., *Arakawa and Schubert*, 1974], we define the entrainment rate (α) as the fractional increase of mass with height (units of %/km). The altitude-dependent change of the trace gas concentration is written as follows:

$$\partial X_{core}/\partial z = \alpha(X_{BKG}X_{core}), \quad (4)$$

where X_{core} and $X_{(BKG)}$ refer to the trace gas concentrations inside the core and in the background, respectively. The term α can be determined iteratively by integrating the equation from the BL to the outflow level. In our analysis, we employ the nonsoluble and passive tracers X (*n*-butane, *i*-butane, *n*-pentane, *i*-pentane, and in the case of the 29 May storm *n*-hexane and *n*-heptane) to determine α. This is accomplished by calculating the dilution of the tracers in successive 1 km altitude bins due to entrainment of background cloud-free air, $X_{(BKG)}$, into the storm core in each altitude bin up to the outflow region, which is equivalent to integrating equation (4). The 1 km altitude bin step size was selected since it represents a good trade-off between vertical resolution and sufficient number of points in each altitude bin. We determine $X_{(BKG)}$ from the median tracer concentrations measured on the DC-8 at each 1 km altitude bin when the aircraft videos and cloud probe indicate sampling in cloud-free air. Rather than use measurements exclusively when the DC-8 ascended from storm base to anvil outflow, which would be based upon a very restricted data set, we tabulate median values for the entire sampling day. The value for each of the tracers in each altitude bin *i* (X_i) is calculated from equation (5):

$$X_{(i)} = (1 - \alpha)X_{(i-1)} + \alpha X_{(BKG)i} \quad (5)$$

The first altitude step in this determination is the 1 km bin range just above the boundary layer IF altitude bin (1–2 km for all DC-8 storm IF measurements; except 11 June where the IF is in the 0–1 km bin; and the 6 June GV IF, where the IF is in the 2–3 km bin). The value of α is iteratively adjusted until the calculated $X_{(i)}$ in the OF ($(X_{core})_{calc, \alpha}$ in Step 3) is equal to our anvil OF measured concentration ($(X_{core})_{meas., t=0}$) for each tracer when extrapolated to the core. The value of α is determined for each of the tracers, and an average and standard deviation are determined. Figure 6 shows a conceptual diagram of this approach for boundary layer IF altitudes in the 1–2 km range and OF altitudes in the 10–11 km range.

The final step in our analysis (Step 4, Figure 6) employs the α value thus determined to calculate the value of $(Y)_{calc, \alpha}$, which represents the entrainment diluted CH_2O value in the OF core before scavenging in accordance with equation (6):

$$Y_{(10-11)} = (1 - \alpha)Y_{(9-10)} + \alpha Y_{(BKG)10-11} = Y_{core\ calc,\ \alpha} \quad (6)$$

This value represents $[CH_2O]_{Anvil\ core\ calc}$ in equation (2) and tabulated in Table 4a. The CH_2O SE is determined from equation (2) employing $[CH_2O]_{Anvil\ core\ calc}$ and the value of $[CH_2O]_{OF\ measured}$, which in Figure 6 (Step 4) is represented by $(Y_{core})_{meas., t=0}$ and tabulated in the fourth column of Table 4a. For clarity, we show here equation (2) again:

$$SE = \frac{\left\{[CH_2O]_{Anvil\ core\ calc.} - [CH_2O]_{OF\ measured}\right\}}{[CH_2O]_{Anvil\ core\ calc.}} \quad (2)$$

It is important to note that in this approach the entrainment changes with altitude, due to changes in the background concentrations that entrain into the convective core. However, this approach implicitly assumes

Table 4a. Determined Parameters Employed in CH$_2$O Scavenging Efficiency Calculations Using the Altitude-Dependent Entrainment Method[a]

Storm	IF/OF Source	[CH$_2$O]$_{IF}$	[CH$_2$O]$_{OF\ extrap\ t=0}$	OF/IF	[CH$_2$O] $_{Anvil\ core\ calc.}$	α
5/29/12	DC-8 IF	4601 ± 526	1093 ± 55	0.24	2392 ± 213	7.6 ± 1.0
	DC-8 and GV OF	(3898 ± 649)[b]			(2047 ± 179)[b]	7.3[c] ± 3.3
					2583[c]	
6/6/12	DC-8 IF	1610 ± 260	575 ± 84	0.36	1204 ± 65	4.1 ± 0.7
	GV OF					
	GV IF	1694 ± 82	657 ± 43	0.39	1257 ± 69	4.1 ± 0.7
	DC-8 OF					
6/11/12	DC-8 IF	4375 ± 702	1524[d] ± 102	0.35	2782 ± 311	4.4 ± 1.0
	GV OF					
5/21/12	DC-8 IF	2410 ± 480	237 ± 27	0.10	1272 ± 268	8.9[e] ± 2.7
	GV OF					
6/22/12	DC-8 IF	1667 ± 194	841 ± 309	0.50	1349 ± 102	3.0 ± 1.1
	DC-8 OF					

[a]All concentrations are in pptv. The Anvil core calc. (sixth column) CH$_2$O values represent the entrainment diluted CH$_2$O values in the anvil core without scavenging (equation (6)) while the [CH$_2$O]$_{OF\ extrap\ t=0}$ (fourth column) are the measured values extrapolated to the anvil core at time = 0 before dilution. For 29 May, two different [CH$_2$O]$_{IF}$ concentrations are used: 4601 pptv (time period 23:10:21–23:15:53, Table 3) and 3898 pptv (23:00:30–23:15:53). The DFGAS and corrected CAMS intercept values weighted by the number of points in the regressions produced the [CH$_2$O]$_{OF\ extrap\ t=0}$ shown here. See text for more detailed definitions of the various terms. The entrainment value α has units of %/km. The OF/IF is the CH$_2$O concentration ratio determined from the fourth column divided by the third column.
[b]CH$_2$O concentration based on entire IF period of 23:00:30–23:15:53.
[c]Using variable 1 km level entrainment rates from WRF tracer simulations (see *Barth et al.* [2016]).
[d]TOGA OF measurements on GV corrected to DFGAS on DC-8 (see text).
[e]Entrainment based only on butanes.

a constant entrainment rate α with altitude, much like the three-component and two-component mixture models of *Borbon et al.* [2012] and *Cohan et al.* [1999], respectively. In the sections that follow, we will further discuss this and any potential errors associated with this assumption.

4.3. Butane Ratio Method

In this approach, we also employ the outflow time estimates just discussed. We extrapolate the ratio of CH$_2$O/n-butane measured at various times in the outflow to time 0 at the storm core (see Table 4b). This value is then compared to the average CH$_2$O/n-butane measured in the storm inflow to arrive at a SE employing equation (7):

$$SE = \frac{\left\{[CH_2O/n\text{-butane}]_{IF} - [CH_2O/n\text{-butane}]_{OF\ meas.,\ t=0}\right\}}{[CH_2O/n\text{-butane}]_{IF}} \qquad (7)$$

We choose n-butane since it shows the largest enhancement of the various tracers selected. Since n-butane is neither reactive nor soluble, any changes in its concentration during transport from inflow to outflow are

Table 4b. Determined CH$_2$O/n-Butane Relationships Used in the Butane Ratio Method of Determining CH$_2$O SEs

Storm	IF/OF Source	[CH$_2$O/n-Butane]$_{IF}$	[CH$_2$O/n-Butane]$_{OF\ extrap\ t=0}$
5/29/12		2.88 ± 0.22	1.42 ± 0.09
6/6/12	DC-8 IF	5.34 ± 0.75	2.41 ± 0.35
	GV OF		
	GV IF	5.65 ± 0.39	2.14 ± 0.12
	DC-8 OF		
6/11/12	DC-8 IF	17.13 ± 9.7	5.96 ± 0.37
	GV OF		
5/21/12	DC-8 IF	13.40 ± 2.3	2.59 ± 0.42
	GV OF		
6/22/12	DC-8 IF	8.88 ± 1.12	5.09 ± 1.9
	DC-8 OF		

assumed to arise strictly from dilution by lateral entrainment. This is valid as long as there are no additional changes from air masses of vastly different origins between inflow and outflow. It should be noted that this assumption is also important for the first approach. However, the added value of the butane ratio method is that it eliminates the explicit determination of α discussed in the previous section and the underlying assumption of a constant α value with altitude. Calculating CH_2O SEs exclusively from CH_2O/n-butane ratios, however, comes at the expense of more limited information content, which in turn does not allow us to investigate the dependence of SE as a function of entrainment. In addition, in some cases the CH_2O/n-butane ratio measurements in the IF show a much larger variance than the CH_2O measurements alone due to low n-butane values (11 June storm case), and this produces SE determinations with larger imprecisions. Therefore, both methods provide complimentary information, which becomes particularly valuable when both methods yield similar results.

To ensure that inflow and outflow time periods are coherently related (i.e., no additional changes from air masses of vastly different origins between inflow and outflow), we further employ the ratios i-butane/n-butane and i-pentane/n-pentane. Again, this is important to ensure that CH_2O SEs from both the altitude-dependent entrainment and butane ratio methods are accurate. More specifically, these ratios provide evidence that the outflow regions are not significantly perturbed by air parcels from locations other than the BL inflow regimes considered here. These ratios take advantage of the fact that the hydrocarbon pairs are relatively constant for a given source, vary from source to source, and have similar OH reaction rate constants. Over the temperature extremes encountered in the BL and the UT, approximately 300 K to 225 K, respectively, the ratio of OH rate constants for i-/n-butane varies from 0.88 to 1.06, and the corresponding ratio for i-/n-pentane varies from 0.94 to 1.12 [*Calvert et al.*, 2008]. Thus, for fresh air masses from a given source region, the two ratios should only marginally change from their source ratios and will increase as the n-isomers decay slightly faster in the aging air masses. Since vertical transport times in these storms are on the order of 10–30 min, most of this aging stems from lateral entrainment of aged background air into the storm columns. We will show the utility of examining such ratios in section 4.5 when we discuss the five storm cases.

4.4. WRF-Chem Modeling Approach

In the case of the 29 May storm, we also employed a more sophisticated approach based upon high-resolution simulations with the Weather Research and Forecasting model with Chemistry (WRF-Chem) [*Grell et al.*, 2005]. This is a fully coupled meteorology-chemistry-transport model supported at the NOAA Earth Systems Research Laboratory and the NCAR Mesoscale and Microscale Meteorology division. A full description of this model as applied to DC3 analysis is the topic of another paper by *Bela et al.* [2016], and we only provide here an overview of WRF-Chem as applied to CH_2O uptake. The WRF-Chem simulations are driven by the North American Mesoscale Analysis (NAM-ANL) with prestorm Lightning Data Assimilation (LDA) based on *Fierro et al.* [2012], and a combination of DC-8 inflow and free/upper troposphere measurements and the Model for Ozone and Related chemical Tracers, version 4 (MOZART-4) [*Emmons et al.*, 2010] global chemistry model forecasts. The chemistry in WRF-Chem uses the EPA 2011 anthropogenic emissions inventory, the Model of Emissions of Gases and Aerosols from Nature (MEGAN) [*Guenther et al.*, 2006], and the Fire Inventory from NCAR (FINN) model [*Wiedinmyer et al.*, 2011]. The trace gas chemistry and aerosols are represented with the MOZART chemical mechanism [*Emmons et al.*, 2010] and Goddard Chemistry Aerosol Radiation and Transport (GOCART) [*Chin et al.*, 2002] aerosol scheme with aerosol direct radiative effects, respectively. Wet deposition for the MOZART trace gas chemistry in the community version of WRF-Chem follows the *Neu and Prather* [2012] (NP2012) scheme, which estimates wet deposition based only on the gas-phase mixing ratios of a trace gas. This scheme estimates trace gas removal by multiplying the effective Henry's law equilibrium aqueous concentration by the net precipitation formation (conversion of cloud water to precipitation, minus evaporation of precipitation). For mixed-phase conditions ($258 \, K < T < 273 \, K$), gases like CH_2O can be degassed from hydrometeors to the gas phase as the phase of water changes from cloud water to ice, snow, or graupel while the air mass ascends and cools in the storm core. The standard NP2012 scheme accounts for this only for species for which ice deposition is included (HNO_3) by removing from the gas phase only 50% of the amount predicted by Henry's law. In NP2012 for mixed-phase conditions, CH_2O is completely degassed from the condensed phase back into the gas phase, and this results in reduced CH_2O SEs. To quantify the impact of ice retention on CH_2O scavenging efficiency, sensitivity simulations were conducted with WRF-Chem, varying the CH_2O fraction retained in ice (r_f). Simulations were carried out with no scavenging, and with scavenging with r_f values equal to the following: 0 (CH_2O completely

Table 5. CH_2O Scavenging Efficiency Determinations (%) Based Upon Three Methods: The Altitude-Dependent Entrainment Model (Alt. Dep. Entrainment Model), Comparisons of CH_2O/n-Butane Measurements in the Outflow to Those in the Inflow (Butane Ratio Method), and WRF-Chem Simulations With Scavenging Turned on (Ice Retention Factor = 0) and Off[a]

| | | CH_2O Scavenging Efficiency (SE) | | |
Storm	IF/OF Source	Alt. Dep. Entrainment Model	Butane Ratio Method	WRF-Chem
5/29/12	DC-8 IF	54% ± 5%	51% ± 5%	53%[d]
	DC-8 and GV OF	(47% ± 5%)[b]		
		58%[c]		
6/6/12	DC-8 IF	52% ± 7%	55% ± 9%	
	GV OF			
	GV IF	48% ± 3%	62% ± 3%	
	DC-8			
	OF			
6/11/12	DC-8 IF	48%[e] ± 7%	67%[e] ± 20%	
	GV OF			
5/21/12	**DC8 IF**	**81 ± 5%**	**81% ± 5%**	
	GV OF			
6/22/12	DC-8 IF	38 ± 23%	43 ± 23%	
	DC-8 OF			

[a]For 29 May the IF periods of Table 3 were used for all three determinations, but we also show in parenthesis the results using the entire BL period indicated in footnote b below. 29 May, 6 June, 11 June, and 22 June are all strong convective cases while the 21 May is a weak convective case. The 21 May results are given in boldface to highlight that the SE determinations are less reliable since the IF and OF were not coherently related (see text).
[b]SE employing the entire DC-8 BL IF region on 29 May (23:00:30–23:15:53).
[c]Employing variable altitude entrainment rates from WRF tracer simulations.
[d]Calculated with fraction retained in ice $r_f = 0$ (complete degassing); when $r_f = 0.25, 0.5, 0.64$, and 1.0, we calculate SEs = 97 to 99%.
[e]11 June SEs corrected for estimates of CH_2O production from isoprene production and destruction from photolysis and reaction with OH.

degassed); 0.25, 0.50; 0.64; and 1.0 (0% degassed). The value of $r_f = 0.64$ in this sensitivity simulation is from the modeling study of *Leriche et al.* [2013], who used the same value as for H_2O_2 from *Voisin et al.* [2000].

The SEs were calculated from the WRF-Chem simulation results as follows.

$$SE = [CH_2O_{noscav} - CH_2O_{scav}]/CH_2O_{noscav}, \qquad (8)$$

where CH_2O_{noscav} and CH_2O_{scav} are the model volume mixing ratios of CH_2O near the storm core as defined by the eastern 40 dBZ maximum reflectivity contour for no scavenging and scavenging, respectively. For each time interval (5 min for the DC-8 and 10 min for the GV), the eastern 40 dBZ contour was determined by starting at the location of each flight point and moving due west until locating the easternmost WRF grid cell with $refl_{max} > 40$ dBZ, restricted to the storm of interest (longitude $> -97.9°$ and latitude $> 36.2°N$ for the DC-8 and 36.35°N for the GV). In addition, stratospheric (O_3/CO > 1.25) and cloud-free ($Q_{tot} < 0.01$ g kg^{-1}, where $Q_{tot} = Q_{cloudwater} + Q_{rain} + Q_{ice} + Q_{snow} + Q_{graupel}$, where Q represents the water content in each of the phases) model points were removed, and finally, the points were restricted to the height ranges of the aircraft sampling on each 5 or 10 minute interval (9.43–11.59 km). The mean outflow values of CO from all WRF-Chem model simulations of the 29 May storm were within the error bars of the observations. This offers further supporting evidence that our WRF-Chem model accurately simulates transport during the 29 May storm. Table 5 (to be discussed) tabulates the resulting SEs from the three methods just discussed.

4.5. CH_2O SE Results for Five Storm Cases
4.5.1. The 29 May Central Oklahoma Storm Case
Barth et al. [2015] determined that the thunderstorms over Oklahoma and west Texas sampled by the GV and DC-8 aircraft exhibited moderate to high shear and CAPE (Convective Available Potential Energy). The 29 May Oklahoma storm complex (hereafter referred to as a storm) was a line of severe convective storm cells with a shared anvil, and the storm most extensively studied in the present analysis. The GV sampled the UT convective outflow, with the DC-8 sampling the inflow followed by UT outflow sampling. The storm initiated in northwestern Oklahoma near the Kansas border and propagated to the east-southeast just north of

Oklahoma City. The inflow air came from both the southeast and east. To the east, more scrub oak and forests exist, while central Oklahoma is affected by Oklahoma City and the outflow of the Dallas-Fort Worth metropolitan area. Multi-Doppler analysis of the SMART [*Biggerstaff et al.*, 2005] and NOXP [*Burgess et al.*, 2010] radar data for the 29 May storm provided detailed vertical velocities as a function of altitude within the updraft core of the most severe cell. For the times of interest here, between 23:20 and 23:50 UTC, the main updraft varied in intensity with peak values of 45–60 m/s at 8 km altitude and 30–45 m/s in the 10–11 km outflow region. Based on hundreds of trajectories using the radar-derived wind fields, we deduced a representative transit time of ~ 7 min from cloud base in the 2–3 km region to the 10–11 km outflow region.

As discussed in section 4.2, our storm IF and OF determinations start with an examination of NEXRAD radar images of maximum column reflectivity with aircraft wind vectors (black refers to the DC-8, while red refers to the GV), as shown in Figures 7a–7c. Figures 7a–7c (top rows) depict the GV and DC-8 altitudes as a function of time, while Figures 7a–7c (bottom rows) depict the corresponding aircraft wind vectors superimposed on the storm radar images. The aircraft wind vectors show three things: the wind speeds (vector length), the wind directions (vector orientations), and the aircraft positions (nonarrow origin side of vectors). The vectors are shown for each 1 min period, with the vector numbers indicating the midtime for each 1 min sampling period (i.e., 23:11 refers to measurements from 23:10:30 to 23:11:30). Figure 7a shows the 10 min period spanning 23:00 to 23:10, while Figure 7b shows the next 10 min period (23:10–23:20). Both figures show the DC-8 sampling in the BL between 1 and 2 km, while the GV is sampling in the UT between 11 and 12 km. Figure 7c shows the evolving nature of this storm approximately 40 min later (23:50 to 24:00) with the DC-8 and GV both sampling the OF, between 10 and 11 km and 11 and 12 km, respectively. Both aircraft are sampling the OF from the Central-Central (C-C) and North-Central (N-C) evolving storm cores. Further inspection of the DC-8 IF time periods in Figures 7a and 7b indicate that the latter, and more precisely vectors 1–6 (midtimes: 23:11–23:16), better represent the IF corresponding to the C-C and N-C OF cores in Figure 7c. Table 3 tabulates the precise IF times used here to 1 s resolution (23:10:21–23:15:53) along with the DC-8 and GV OF times on the 1 min data merge sampling periods. At the end of the above IF period, the CH_2O levels began to drop significantly as the DC-8 started its climb to high altitudes.

Distinguishing between these two DC-8 BL segments is important, since as can be seen in the time series plots in Figure 8a, the isoprene, and hence CH_2O, differ significantly between these two BL segments. The average isoprene and CH_2O levels in the two inflow regimes differ by 57% and 31%, respectively. The CO levels also change between these two regions, but the average increase (2.6%) is significantly less. We further highlight in Figure 8a both the DC-8 IF and OF time periods by the shaded regions. Although we believe that the above IF time period best represents the C-C and N-C storm IF, we will also show CH_2O SE results employing the entire BL sampling period from 23:00:30 to 23:15:53, to indicate the sensitivity of our results on the IF time period choice.

As we discussed previously, the OF time periods were identified whenever the aircraft wind vectors pointed away from the storm cores toward the aircraft positions when flying through the anvil, as shown in Figure 7c, and this was supported by numerous other indicators. As stated previously, in most cases measurements directly at the storm core tops could not be acquired for obvious safety reasons. However, the DC-8 aircraft wind vectors #1 and #2 in Figure 7c (midtimes 23:51 and 23:52) represent an exception to our anvil outflow standoff sampling protocol; as can be seen, the DC-8 sampled right on top of one of the storm cores, and the time between aircraft sampling and the closest intense storm core was estimated at 1 min for both time periods using the procedures previously described. The DC-8 encountered a lightning strike from the storm core during the first 1 min measurement period, adding further credence to our short outflow time estimates. The 1 s DFGAS CH_2O measurements averaged 1128 ± 79 pptv and 1194 ± 87 pptv over the 1 min time intervals for vectors #1 and #2, respectively (GPS altitude = 11.1 km). Figure 8b shows the GV OF measurements from this same storm core while sampling at an altitude of ~11.7 km as well as OF measurements from the N-C storm core at the same altitude at times around 24:20.

Figure 9 plots the resulting DC-8 and GV CH_2O measurements (1 min averages with standard deviations) for the C-C and N-C storm cores as a function of estimated storm core outflow times employing the geometric approach previously described. The midtimes during the 1 min sampling periods are shown for select points, and in this analysis, we in essence lump the two outflow storm cores into one grouping for each aircraft. For reference, the averaged DC-8 inflow value highlighted in Figure 8a is plotted on the right-hand axis with its standard deviation. The dark blue and red lines are the linear regression fits of the DC-8 and GV outflow data.
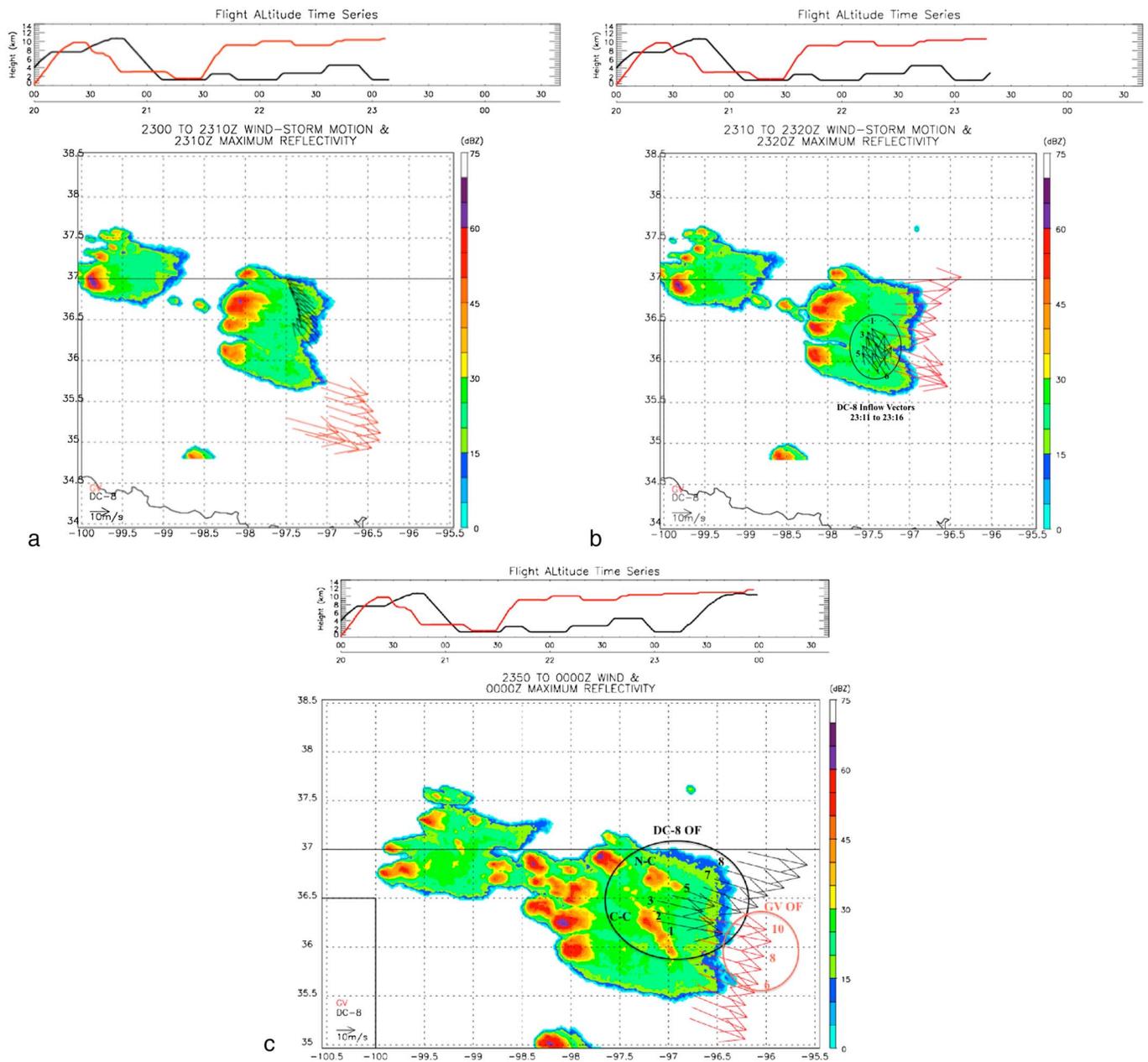
Figure 7. (a) The 29 May storm over Oklahoma (23:00–23:10). The flight altitude time series for the DC-8 and GV aircraft are depicted in Figure 7 (top), while Figure 7 (bottom) depicts the radar images with the DC-8 (black) and GV (red) vectors superimposed. The radar intensities are referenced to the right-hand color scale. (b) The 29 May storm over Oklahoma (23:10–23:20). DC-8 IF vectors 1 through 6 denote midminute sampling times of 23:11 to 23:16. It is important to note that the IF vectors all point in the direction of the C-C and N-C forming storm cores shown in Figure 7c. (c) The 29 May storm over Oklahoma (23:50–24:00) showing select outflow periods for both the DC-8 and GV for the Central-Central (C-C) and North-Central (N-C) storm cores. The DC-8 OF vectors (1 through 8) span the time range 23:51–23:58 (midtimes on 1 min merge). The corresponding GV OF vectors (6–10) span the time range 23:56–24:00. These OF periods represent part of the OF employed in our analysis. Table 3 lists the complete time ranges employed.

The corresponding intercepts, which are highlighted by the larger points on the Y axis, (DC-8 = 991 ± 67 pptv and GV = 1186 ± 87 pptv) represent the CH_2O core values extrapolated to time 0, $(Y_{core})_{meas., t = 0}$. The average of these two values, weighted by the number of points in the regressions, yield a combined DC-8-GV outflow intercept of 1093 ± 55 pptv, and this is tabulated in the fourth column of Table 4a. Nearly identical results are obtained using exponential fits fixed with constant background values. Previously, we discussed the importance of eliminating stratospheric air in our analysis, and the four GV outflow samples highlighted by large
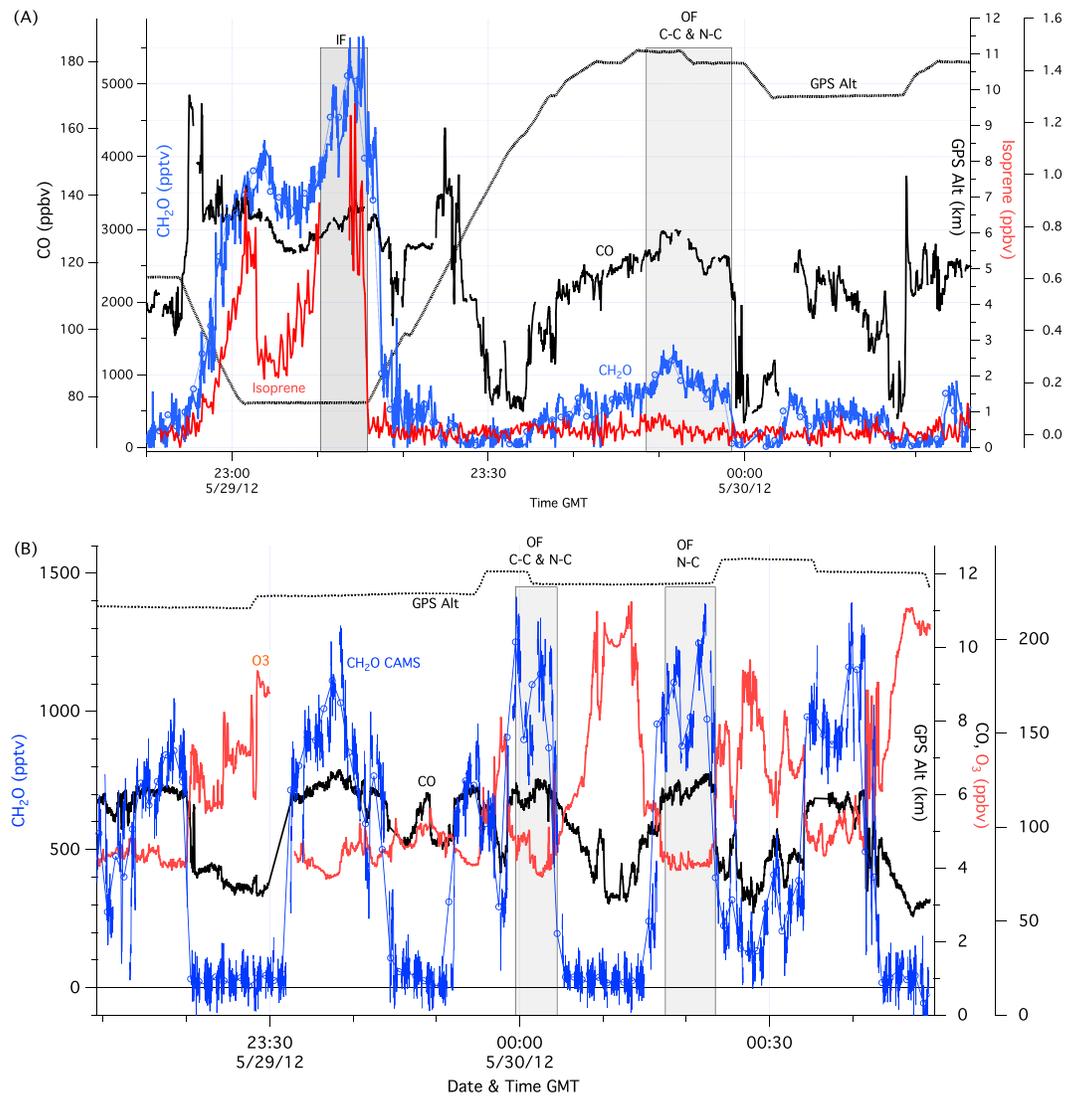
Figure 8. (a) DC-8 29 May storm inflow (IF) and outflow (OF) time series depicting the measurements for: CH$_2$O (1 s data blue lines, 1 min data open blue points) from the DFGAS instrument, isoprene (red) from the PTRMS instrument, and CO (black) from the DACOM instrument. The C-C and N-C OF storm cores refer to the Central-Central and North-Central outflow storm cores shown in Figure 7c. (b) GV 29 May storm outflow time series depicting the measurements for: CH$_2$O (1 s data blue lines, 1 min data open blue points) from the CAMS instrument (not corrected here using regression in Figure 1), CO measurements from Teresa Campos (black lines), and O$_3$ from Andy Weinheimer's group (red lines).

open red circles shown in Figure 9 further reinforce this point. As can be seen, these four points do not fall on the same GV outflow time-dependent apparent decay as the remaining points. Combining the results from the two aircraft is justified here, even though the GV is ~ 1 km higher than the DC-8, since the apparent decays yield similar slopes and intercepts.

Although the data in both regressions show a fair amount of scatter, the time 0 extrapolated DC-8 and GV outflow values are nearly identical within their imprecision limits. This scatter we believe may arise from a number of factors, which include the following: (1) the assumption of linear mixing/dilution/reaction as a function of outflow time, (2) uncertainties in our geometric determinations of outflow times, (3) treating the outflow of separate storm cores (i.e., the N-C, and the C-C) as one unified storm outflow, (4) neglecting the possibility that the measured outflows result from a varying mixture of inflow cores, and similarly (5) neglecting the possibility that the measured outflows may be perturbed to some extent by air parcels from locations other than the BL inflow regimes considered. We minimize this latter possibility using *i-/n*-butane
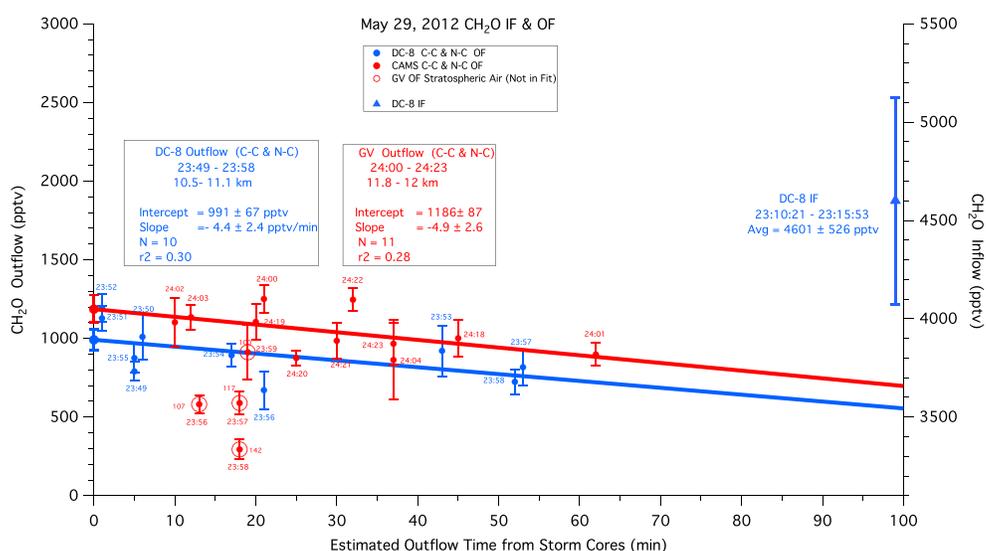
Figure 9. The 29 May storm 1 min outflow measurements acquired by the DFGAS instrument on the DC-8 (blue points) with standard deviations for the C-C and N-C storm cores and by the CAMS instrument on the GV (red points, corrected by the regression results of Figure 1). The times near each point represent the 1 min midsampling times. The dark lines represent unweighted linear regression fits of the DC8 and GV data, and these results are given in the boxes. Four GV points, highlighted by large open red circles, were not included in the fit since the O_3 levels (given next to each point, range 100–142 ppbv, O_3/CO ratio range 0.88–1.7) all indicated stratospheric air. The larger DC8 and GV regression intercept points are also shown on the Y axis at $X = 0$. Also shown (near right-hand axis) is the inflow (IF) CH_2O measurement average acquired by the DFGAS instrument.

and i-/n-pentane. Table 6 tabulates the measured tracer ratios for inflow and outflow for the five storm cases studied here. Table 1 further tabulates the level of agreement for the i-/n-butane and i/n-pentane ratios from the GV TOGA and DC-8 WAS measurements during the five wingtip comparison days. As can be seen, the average point-by-point (TOGA-WAS) difference for both ratios in Table 1 is small, and the standard deviation of these ratios provides a guide in helping us assess whether or not observed inflow and outflow differences are due to atmospheric differences or instrumental differences. The outflow ratios are all extrapolated to time 0 in the same manner as discussed for CH_2O in Figure 9. For the 29 May storm, the inflow and outflow ratios are close and within the (TOGA-WAS) difference standard deviations for the i-/n-butane and i-/n-pentane ratios. By contrast, *Blake et al.* [2015] measured significantly different ratios for air masses influenced by urban, biomass burning, and oil and gas operations, and these are shown in the boldfaced rows at the bottom of Table 6 for reference. The oil and gas plumes from *Blake et al.* [2015] over Texas, Oklahoma, and Kansas, as expected, show ratios close to those measured during the 29 May Oklahoma storm. These results thus add some confidence that the 29 May inflow and outflow regions identified here are not significantly perturbed by source origin differences. We also eliminate the possibility that fire-influenced convection plumes affect our 29 May results. We will discuss this aspect in greater detail in connection with the 22 June storm case.

Based upon the six passive tracers (i,n-butane, i,n-pentane, n-hexane, and n-heptane) and the iterative approach previously discussed, we determine an entrainment rate (α) for the 29 May storm of $7.6 \pm 1.0\%$ km^{-1} (seventh column of Table 4a). This value broadly agrees with entrainment rates (7 to 10%/km) determined from analyzing moist static energy profiles as carried out by *Luo et al.* [2010]. In addition, this value is in excellent agreement with the average entrainment rate of $7.3 \pm 3.3\%$ km^{-1} determined by *Barth et al.* [2016] employing WRF tracer simulations of the 29 May storm. It is important to note that this simulation also determined variable entrainment rates in each 1 km altitude bin, and as will be discussed, these variable 1 km level entrainment rates are also used in the calculation of CH_2O SE.

Table 4a (sixth column) tabulates the resulting $Y_{Anvil\ core\ calc.}$ value of 2392 ± 213 pptv for the 29 May storm based upon the average entrainment rate using equation (6). Applying our determined $Y_{extrap\ t=0}$ value of 1093 ± 55 pptv from Figure 9, we arrive at CH_2O scavenging efficiencies of $54\% \pm 5\%$ (third column of Table 5 converted from fractions to %) for the constant entrainment rate determined from the six hydrocarbon tracers. The 1σ precision limits were calculated from an error propagation analysis using the maximum and minimum

Table 6. Tracer Hydrocarbon Ratios as an Indicator of Air Mass Source Region[a]

Source Region	i-Butane/n-Butane	i-Pentane/n-Pentane
29 May storm DC-8 IF	0.33	0.87
29 May storm DC-8 and GV combined measured outflow extrapolated to t = 0	0.39 ± 0.004	0.89 ± 0.02
6 June storm, combined DC-8 and GV IF	0.40 ± 0.01	1.01 ± 0.05
6 June storm, combined DC-8 and GV OF extrapolated to t = 0	0.39 ± 0.02	0.96 ± 0.03
11 June storm DC-8 IF (22:29:30–22:57:30)	0.57 ± 0.09	1.46 ± 0.12
11 June storm (21:59:30–22:37:30) GV OF extrapolated to t = 0	0.67 ± 0.02	1.44 ± 0.04
21 May storm DC-8 IF (19:30:43–19:38:00)	0.36 ± 0.02	2.22 ± 0.07
21 May storm GV OF (20:50:30–21:14:30) extrapolated to t = 0	0.42 ± 0.02	1.01 ± 0.11
22 June storm DC-8 IF (22:31:27–22:45:54)	0.36 ± 0.01	1.11 ± 0.05
22 June storm DC-8 OF (25:16:30–25:20:30) extrapolated to t = 0	0.46 ± 0.005	1.04 ± 0.01
Urban CA measurements SEAC4RS	**0.53 to 0.67**	**2.9 to 3.3**
Texas, KS/OK oil and gas measurements SEAC4RS	**0.36 to 0.69**	**0.97 to 1.43**
28 U.S. cities	**0.48**	**2.0**
Biomass fire measurements SEAC4RS	**0.26 to 0.27**	**0.31 to 0.37**

[a]All ratios in boldfaced are from *N. Blake et al.* [2015].

values of α. Our SE determination is based upon the IF region shown in Figure 8a and tabulated in Table 3, which we believe more accurately reflects the C-C and N-C OF conditions. However, if we include the entire BL sampling region from 23:00:30 to 23:15:53, the CH_2O SE only changes to 47% ± 5% (given in parenthesis). Employing the variable entrainment rates for each 1 km altitude bin determined from the WRF tracer simulations of *Barth et al.* [2016] in equation (6) yields a $Y_{Anvil\ core\ calc.}$ value of 2583 pptv and a corresponding SE = 58%. Thus, errors associated with assuming a fixed entrainment rate here are small. This is further supported by the results of the butane ratio method, which yields a CH_2O SE = 51% ± 5% (fourth column of Table 5).

Table 5 (fifth column) also shows the WRF-Chem SE result of 53% for the 29 May storm employing an ice retention value of 0% ($r_f = 0$, complete degassing). It is notable that this value is in agreement with the values from the other two approaches assuming that CH_2O is completely degassed upon ice formation. The sensitivity runs with ice retentions > 0, in all four cases produce unrealistically large CH_2O SEs of 97 to 99%. *Bela et al.* [2016] further discusses WRF-Chem modeling results for H_2O_2, CH_3OOH, HNO_3, and SO_2 with various r_f values.

4.5.2. The 6 June Northeast Colorado Storm Case

Plots for 6 June and the remaining four storm cases are given in the supporting information. The 6 June storm over northeast Colorado, like the 29 May case, represents strong convection characterized by high shear and CAPE. The low-level airflow is from the southeast, and upper level flow is from the west. The Colorado storms have high cloud bases with moderate to high anthropogenic VOCs and low biogenic VOCs in the boundary layer. Isoprene levels in the BL over the study area were typically < 200 pptv, as can be seen in Figure S1a and S2b. Other fast-reacting alkenes like ethene (not shown) only attain values of 70 pptv in the inflow. This eliminates the BL inflow heterogeneity encountered in the 29 May storm. On 6 June, isolated convection formed on the apex of the Denver cyclone at about 20:30 UTC, but as the afternoon proceeded, several convective cells formed in the DC3 network. The CSU-CHILL and PAWNEE radars sampled three different storms while the DC-8 and GV sampled the inflow and outflow of two of these storm cells. Sampling during this day was not affected by the large Colorado wildfires that were prevalent later in the month. The linear regression results of Table 7 (to be discussed), where we tabulate CH_3CN versus CO and HCN versus CO slopes, further support this. This will be further discussed in the section describing the 22 June storm.

Figures S1a and S1b and Table 3 show that the DC-8 sampled the inflow from 22:13:40 to 22:25:12 while the GV sampled the storm outflow at various times from 22:20:30 to 22:53:30. The GV then descended to sample the inflow around 23:50:30 to 23:55:30 while the DC-8 ascended to sample the outflow at various times from 23:56:30 to 24:09:30. It is important to note that the DC-8 outflow is split into two distinct periods over this time domain. As can be seen, both the CH_2O and CO drop in Figure S1a over the middle time period from 24:02:30 to 24:07:30. This drop corresponds to a significant increase in measured O_3 (maximum = 195 ppbv and average = 146 ppbv, not shown) as stratospheric air is sampled. Simply calculating an average over the entire DC-8 outflow time span, which includes this stratospheric period, would result in an erroneously low CH_2O outflow value of 364 pptv instead of the extrapolated value of 657 pptv indicated in Figure S2. This in turn would result in an erroneously high CH_2O SE.

In our SE determinations for 6 June, we compare the DC-8 inflows with the GV outflows and the GV inflows with the DC-8 outflows. Such cross-platform comparisons in this case yield optimum results since the inflow and outflow periods are close in time. Like the 29 May storm, the inflow and outflow i-/n-butane and pentane ratios are equivalent within their precisions (Table 6), again suggesting that inflow and outflow regions identified here are not significantly perturbed by source origin differences. For this storm, our analysis determined a 4.1 ± 0.7%/km entrainment rate (Table 4a) resulting in SEs of $52\% \pm 7\%$ and $48\% \pm 3\%$, for the DC-8 inflow-GV outflow and GV inflow-DC-8 outflow comparison pairs. The corresponding SE values for the butane ratio method yields $55\% \pm 9\%$ and $62\% \pm 3\%$. Not only are these four values consistent with one another but also are also consistent with the various SE values for the 29 May storm.

4.5.3. 11 June MCS Over the Southeast Case

On 11 June we sampled an MCS over Arkansas, southern Missouri and Illinois, and northern Mississippi. At 00 UTC 12 June the surface-based CAPE at Jackson, Mississippi, was 3409 J kg^{-1} and a moderate vertical wind shear (10 m/s for the 0–6 km altitude range) was determined for the thermodynamic environment of this storm. However, the dense forested region produces very high levels of biogenic VOCs. Isoprene and CH_2O levels in the BL were both as high as 6 ppbv, and like the 29 May case, this produces quite a bit of variability in the inflow CH_2O levels. In addition, as can be seen in Figure 4, there is a geographic disparity between the DC-8 inflow region and the GV outflow regions, and this presents some challenges in properly relating inflow to outflow legs. Unfortunately, because it was anticipated that the MCS would dissipate during the day, the storm was not the sole focus of the 11 June flight. CAMS was not available on this day, so TOGA CH_2O measurements normalized to DFGAS via the regression fit of equation (2) were employed.

The inflow and outflow legs were determined employing the procedures previously discussed. Although the GV outflow leg (21:28 to 21:48) in front of the storm appears to be sampling convective outflow air, the i-/n-pentane ratio for this outflow leg when extrapolated to time 0 in the storm core yields a value of 0.99 ± 0.06, which is significantly different than the 1.46 ± 0.12 inflow value (see Table 6). Thus, the measurements from this GV flight leg are not used in the analysis. In addition, the majority of the convective outflow air is transported to the rear of the MCS [*Houze et al.*, 1989], which is where the 21:59:30–22:37:30 GV outflow leg occurs (highlighted in Figure 4 over northern Arkansas and southeastern Missouri). When the i-/n-pentane and butane ratios in this outflow leg are compared to the 22:29:30–22:57:30 DC-8 inflow leg (over southern Arkansas and northwestern Mississippi), then we obtain equivalent i-/n-pentane and butane ratios within their measurement precisions, despite the fact that the legs are separated geographically. Figure S3 shows the outflow CH_2O values as a function of estimated outflow time. The estimated entrainment rate for this storm is 4.4 ± 1.0%/km. The resulting SEs for the altitude-dependent entrainment and butane ratio methods are $45\% \pm 7\%$ and $65\% \pm 20\%$, respectively. These results are equivalent with one another and with the other storm cases within the measurement precisions, albeit the differences are larger here than the previous cases. Much of the uncertainty may arise from not having a complete data set in and near the MCS. This is especially important for the clear-sky vertical profiles because air is often ingested into an MCS from above the boundary layer [*Cotton et al.*, 1995].

4.5.4. The 21 May Weak Convection Over Northern Alabama

On 21 May we sampled weak convection over northern Alabama and southern Tennessee, and this provides contrast to the previous strong convective cases. Table 2 shows a factor of ~2 times lower maximum vertical velocity for this storm compared to 29 May and 6 June. Boundary layer isoprene levels, which averaged 463 pptv in the inflow and reached a maximum of 986 pptv, were considerably lower than the values measured on 11 June and 29 May. The corresponding inflow CH_2O levels attained moderate levels of 2410 pptv but very low outflow levels of 237 pptv (see Table 4a and Figure S4). The estimated entrainment rate is 8.9 ± 2.7%/km. The resulting CH_2O scavenging efficiency from both the altitude-dependent entrainment and butane ratio methods is 81 ± 5%. The SE is clearly higher than the three previous strong convective cases. In addition, unlike the previous cases, the pentane ratio for the outflow is vastly different than the inflow (Table 6) and the difference (1.21) is 3.5 times higher than the 0.35 1σ value listed in Table 1 for the TOGA-WAS comparisons. The inflow ratio of 2.22 ± 0.07 is more indicative of urban city air rather than lower ratios indicative of air influenced by oil and gas drilling operations. The outflow pentane ratio of 1.01 ± 0.11 is clearly different and suggests significantly more aged air. This disparity also adds a great deal of uncertainty to our 21 May results, despite the fact that the i-/n-butane ratios are not that different between IF and OF. As can be seen, the i-/n-butane ratios between urban and oil and gas drilling operations overlap [*Blake et al.*, 2015] and

Table 7. DC-8 CH_3CN and HCN Regression Slopes With CO During Outflow Periods

Date	OF	Slope[a] (CH_3CN/CO)	R^2	N	Slope[a] (HCN/CO)	R^2	N
29 May	DC-8	-2.11 ± 0.59	0.15	73	1.80 ± 0.37	0.05	416
	GV	0.29 ± 0.04	0.04	207	-2.70 ± 0.22	0.42	207
6 June	DC-8	0.57 ± 0.78	0.10	66	2.87 ± 1.21	0.03	420
	GV	0		59	0		59
11 June	GV	0.97 ± 0.067	0.26	609	-1.19 ± 0.20	0.06	609
21 May	GV	0.096 ± 0.026	0.04	346	-	-	-
22 June	DC-8	1.24 ± 0.42	0.24	30	3.44 ± 0.51	0.31	103

[a]Weighted average of linear regression slopes and r^2 values for the indicated outflow segments. The CH_3CN measurements are from the Wisthaler group PTRMS instrument, and the HCN measurements are from the Wennberg group Chemical Ionization Mass Spectrometer instrument [*Crounse et al.*, 2009].

in this case are not as useful as the pentane ratios. However, as we will see in the 22 June storm, achieving similar *i*-/*n*-pentane and butane ratios between IF and OF is a necessary but not sufficient condition to ensure accuracy in SE determinations.

4.5.5. Fire-Influenced Convection Over Colorado and Nebraska on 22 June

Our final storm case examined here is 22 June. As discussed by *Apel et al.* [2014], the High Park fire west of Fort Collins, Colorado, had been burning since 9 June, and both airplanes intercepted convection influenced by significant biomass burning on numerous occasions throughout 22 June/23 June. This provided an opportunity to briefly investigate the effects of fire emissions on SE determinations. Figure S5 shows DC-8 time series traces for CH_2O, CO, and acetonitrile (CH_3CN) IF and OF time periods, with the OF from the developing southern storm. *Apel et al.* [2014] discuss the use of CH_3CN and HCN as sensitive tracers of fire-influenced plumes employing regression plots of both gases to CO. On the DC-8 the CH_3CN measurements were from the PTRMS instrument from the Wisthaler group while HCN measurements were from the CIMS instrument from the Wennberg group [*Crounse et al.*, 2009]. As discussed by *Apel et al.* [2014], the regression slopes from the DC-8 data clearly intercepted fire plumes at two different times and resulted in HCN/CO slopes of 6.04 ± 0.43 (pptv/ppbv) and 6.34 ± 0.32 and CH_3CN/CO slopes of 2.55 ± 0.18 (pptv/ppbv) and 2.57 ± 0.08. As further discussed by *Apel et al.* [2014], these values fall within the ranges found in the recent literature (2.4–12.8 for HCN/CO and 1.1–4.3). Even though the OF profiles shown in Figure S5 do not appear on the surface to be influenced by fire emissions, in contrast to time periods before and after the highlighted OF region, our regression slopes tabulated in Table 7 appear to show some fire influence in the OF. This is in spite of the consistency in the *i*-/*n*-pentane and butane ratios between IF and OF (Table 6). In contrast to all other sampling days, the OF HCN/CO and CH_3CN/CO regression slopes on 22 June yield values within the fire-influenced emission ranges listed by *Apel et al.* [2014, and references therein] with moderate r^2 correlation values. For this case, the derived entrainment rate is 3.0 ± 1.1%/km (Table 4a), and this results in CH_2O SEs of 38 ± 23% and 43 ± 23%, for the altitude-dependent and butane ratio methods, respectively (Table 5). The large SE imprecisions are reflective of the large relative imprecisions in the extrapolated values back to the storm core for $[CH_2O]_{OF\ extrap\ t=0}$ (Table 4a) and $[CH_2O/n\text{-butane}]_{OF\ extrap\ t=0}$ (Table 4b) due to the limited number of points ($N = 4$ for CH_2O and $N =$ for CH_2O/n-butane ratios). It is notable that the above SE results for 22 June, although slightly lower, are in the range of the 29 May, 6 June, and 11 June results. Since the 22 June OF periods appear to be somewhat fire influenced, in contrast to the IF (CH_3CN/CO slope $= -1.4 \pm 0.8$, $r^2 = 0.03$; HCN/CO slope $= 2.1 \pm 0.4$, $r^2 = 0.04$), we cannot rule out the possibility that CH_2O production from the fire exerts a small differential effect on the OF for the southern storm relative to the IF. As can be seen from Figure S5, the OF from the northern storm, which appears at earlier times shows extremely large CH_2O production from the fire. This could explain the apparent lower SEs. Hence, extreme caution is advised whenever one studies convection in and near fire plumes. In addition, as postulated by *Tabazadeh et al.* [2004], CH_2O may be produced heterogeneously from methanol in biomass smoke plumes that encounter clouds.

5. Estimates of CH_2O Destruction and Production in the Storm Cores and Their Effects on the CH_2O SE Determinations

Our extrapolation approach previously described takes into account changes in CH_2O concentrations in the anvil OF in the time between aircraft sampling and the storm core. In this section we separately estimate the

contributions of CH_2O destruction and production on its SE during convective transport in the storm core. The extrapolated measured CH_2O concentrations back to the storm core, $[CH_2O]_{OF\ extrap\ t=0}$, must be modified by these processes, and this section estimates maximum corrections to these values, and hence, the CH_2O SEs.

5.1. Estimates of CH_2O Destruction by Photolysis and Reaction With OH

Destruction of CH_2O can occur from both photolysis and reaction with OH. Although there can be some uncertainty in estimating these contributions, in the present study, we arrive at upper limit estimates for these contributions based upon DC-8 measurements of photolysis frequencies provided by Sam Hall and colleagues (calculated using the CAFS CCD Actinic Flux Spectroradiometers) and OH concentrations provided by Bill Brune and his group (Airborne Tropospheric Hydrogen Oxides Sensor, ATHOS, based on laser-induced fluorescence) when flying through clouds. The cloud indicators previously discussed were used here. We note that these in-cloud time periods do not precisely match the photolysis and OH conditions present in the actual cores of strong convection, which are significantly more opaque, but they provide upper limit estimates for each altitude. These measurements even provide realistic estimates for in-cloud photolysis frequency enhancements at the upper altitudes where we do fly in the anvil OF. The CH_2O loss rate is calculated in 1 km altitude steps (i) and these are summed from the altitude step above the BL IF to the anvil OF layer from:

$$\Delta[CH_2O]_{destruction,\ i} = \sum \left(1 - \exp^{-\left(k[OH]i\ ^*(t)i\ +\ (jm)i+(jr)i\right)}\right). \qquad (9)$$

Here k is the OH reaction rate for CH_2O destruction ($CH_2O + OH \rightarrow H_2O + HCO$) and is equal to $8.5 \times 10^{-12}\ cm^3\ molecule^{-1}\ s^{-1}$ for the $220\ k$–$298\ k$ range [*Sander et al.*, 2011], the $[OH]_i$ is the ith altitude binned median measured LIF OH concentration, t_i is the reaction time for each altitude bin i, and $(jm)_i$ and $(jr)_i$ are the corresponding altitude binned median CH_2O molecular ($CH_2O + h\upsilon \rightarrow H_2 + CO$) and radical ($CH_2O + h\upsilon \rightarrow HCO + H$) photolysis frequencies, respectively. For 29 May, we have time estimates for each altitude time step, since vertical velocities were explicitly determined by the University of Oklahoma (D. Betten and M. I. Biggerstaff) for the storm cores under consideration. The overall time in the storm core from 2 km to the 10–11 km OF was estimated at ~ 7 min, and a summation of the CH_2O destruction rates at each time step resulted in a maximum overall destruction value from photolysis and reaction with OH of 2% during vertical transport in the storm core. This is similar to the 4% estimate deduced by *Borbon et al.* [2012] for strong MCS convective cases. An increase in the $[CH_2O]_{OF\ extrap,\ t=0}$ value of 1093 pptv by 2% only translates to a change in CH_2O SE from equation (2) of 0.9%, from 54 to 53%, when rounded off. This small decrease is approximately countered by a similar small increase due to estimated CH_2O production in the storm core from isoprene oxidation (discussed in the next section).

Table 2 lists the maximum vertical velocities for three of the five storm cases, and we expect similar small CH_2O destruction rate corrections for four of the five storm cases, which are characterized as severe or supercell convection. For 11 June, we estimate a CH_2O destruction rate of 5%, assuming the same vertical velocities in each 1 km altitude bin as 29 May. For the weaker air mass thunderstorm of 21 May, we estimate this correction by scaling the transit time in each layer by the ratio of the maximum measured vertical velocities (45/20). Here we use the lower end of the velocity scale for the 29 May storm. This produces an overall storm core vertical transport time of ~ 15 min, and an overall maximum 14% correction estimate to the $[CH_2O]_{OF\ extrap,\ t=0}$ value of 237 pptv, which results in a maximum change in SE from 81% to 79%, which is well within the 5% imprecision estimate in Table 5.

5.2. Secondary Production of CH_2O From Hydrocarbon Oxidation in the Storm Cores

In their studies of midlatitude continental convection, *Fried et al.* [2008b] provide convincing evidence for the importance of photochemically produced CH_2O from its precursors relative to direct transport of CH_2O from the boundary layer. However, the convection studied by *Fried et al.* [2008b] was both much weaker and older than the strong convection cases studied here. Based upon NASA Langley photochemical box model results shown in Figure 7 of *Fried et al.* [2008b], the enhanced CH_2O production rate from the convective cases they studied in the 10–12 km altitude range was ~1.5 pptv/min. For the ~7–15 min convective transport time estimates of the present study, this amounts to an insignificant CH_2O production of 10–23 pptv during transport. Nevertheless, we estimate here an upper limit for secondary production of CH_2O. Of the cases studied here,

oxidation of isoprene by OH is the largest potential source of secondary CH_2O during convection. Since CH_2O is simultaneously produced by this mechanism while it is being scavenged by liquid droplets, the true scavenging efficiency would be higher than that determined here. *Borbon et al.* [2012] also considered this possibility and estimated photochemical production contributions ranging between 13% and 33% for two different regions, with the latter representing a tropical forest region with isoprene levels of 604 pptv. In the present study, isoprene was only high enough to be potentially important during the 29 May storm over Oklahoma and the 11 June storm over Missouri and Arkansas. The average and peak isoprene values for the 29 May IF are 702 pptv and 1227 pptv, respectively. The corresponding values for the 11 June storm core are 2580 pptv and 6522 pptv. The only other storm where the inflow isoprene was significantly above zero in the IF was 21 May where the average IF isoprene was 188 pptv and the OF ~ 1 pptv. In contrast to *Borbon et al.* [2012], where the reacted isoprene had to be calculated based upon a photochemical model, the present study employs direct measurements of isoprene in both the inflow and outflow regions to arrive at the potential CH_2O contribution from isoprene oxidation via equation (10):

$$CH_2O_{Isoprene} = 0.18 \times \Delta Isoprene \times SE_{CH_2O}. \tag{10}$$

Here the ΔIsoprene is calculated using the average inflow values diluted by lateral entrainment of background air in the same manner as $Y_{Anvil\ core\ calc.}$ in equation (6) minus the measured outflow values extrapolated to time 0, exactly analogous to our CH_2O SE calculations. At high NO levels typically greater than many hundreds of pptv, the mean fractional yield of CH_2O from the first oxidation stage of isoprene is 0.61. However, during both storms the NO levels averaged less than 10 pptv, and in this case isoprene hydrogen-peroxide (ISOPOOH) is formed and the resultant first generation isoprene formation of CH_2O is significantly reduced. Fortunately, we were able to directly acquire a value for this reduced fractional yield during the 30 August 2013 flight, the so-called *isoprene volcano* flight, in the SEAC⁴RS study. Here the CH_2O-isoprene slope was obtained while flying in the isoprene-rich boundary layer over southern Missouri and northern Arkansas with NO levels less than 100 pptv. A regression plot resulted in a CH_2O-isoprene slope of 0.18 ± 0.007, and this value is used in equation (10). The last term, the SE_{CH2O}, accounts for the fact that the CH_2O produced from isoprene is partially removed by wet scavenging. We use an averaged CH_2O SE of 54% and 55% for the 29 May and 11 June 11 storms, respectively, for this purpose.

For the 29 May storm we estimate a negligibly small CH_2O production from isoprene of 29 pptv. As mentioned in the previous section, this small potential CH_2O production is approximately countered by a similar decrease (22 pptv) due to photolysis and reaction with OH, and therefore, no net corrections were applied to CH_2O SEs in Table 5. By contrast, the 11 June storm with significantly higher boundary layer isoprene levels yields an estimated CH_2O production from isoprene of 149 pptv. This production is countered by an estimated CH_2O loss of ~ 72 pptv due to photolysis and reaction with OH during vertical transport, resulting in a net correction of ~ 77 pptv to the $[CH_2O]_{OF\ extrap,\ t = 0}$ value in Table 4a (correction subtracts from this value). This translates to a modified SE of 48% from the reported value of 45% for the altitude-dependent entrainment method and 67% from 65% for the butane ratio method. These estimated corrected values are given in Table 5.

6. Discussion of CH_2O SEs and Comparisons With Other Mixing Models

6.1. Discussion of CH_2O SEs in This Study

The CH_2O scavenging efficiencies tabulated in Table 5 are remarkably consistent for the three strong convective cases (29 May, 6 June, and 11 June), both between storms and between the various approaches. The CH_2O scavenging efficiency ranges between 48% (47% if we consider the expanded IF region for 29 May) and 67%, and with one exception, the various approaches are in agreement within the stated 1σ estimated precisions. The average of the four 29 May values for the most likely IF time period of Table 3 (i.e., the average of 54%, 51%, 53%, and 58%) produces a combined average of 54 ± 3% ($n = 4$). The corresponding combined average for 6 June is 54 ± 6% ($n = 4$) and for 11 June is 58% ± 13% ($n = 2$), with the imprecision limits reflecting the standard deviation of the combined mean and not the individual imprecisions. The SEs from these three storms are remarkably similar. The corresponding average for the 22 June storm, which to some extent may be influenced by fire emissions, produced a lower CH_2O SE of 41 ± 4%, with much larger individual imprecisions. It is noteworthy that the simplified butane ratio method yields very similar values as

the altitude-dependent entrainment model in almost every case. As stated previously, the former method implicitly includes dilution and entrainment during transport, while in the latter the column-averaged entrainment value must first be determined. Thus, errors arising from a variable entrainment rate with altitude must be small, and this has been further confirmed for the 29 May storm employing variable entrainment rates determined by WRF tracers. In addition, the agreement for the various approaches for the three strong convection cases studied is consistent with the similar maximum vertical velocities for 29 May and 6 June (Table 2), which plays an important role in governing scavenging efficiencies. As discussed by *Barth et al.* [2007], vertical velocity controls the residence time in contact with liquid water. However, the factor of ~ 6 difference in maximum ice water content measured in the outflow between the two storms is not consistent with the nearly equivalent SEs. This would suggest that either the measured ice water content in the outflows between the two storms do not reflect those in the storm cores during vertical transport or that ice water content is not a controlling variable in governing SEs.

The weaker convection on 21 May with a factor of ~ 2 lower maximum vertical velocity, and hence longer contact time with liquid water, yields a significantly higher average CH_2O SE of 81% ± 5% compared to the other storms. However, as mentioned, the disparity in the *i-/n*-pentane ratios between inflow and outflow adds uncertainty to this value. The lower outflow ratio (1.01 ± 0.11) compared to the inflow (2.22 ± 0.07) suggests that the outflow is significantly influenced by well-aged air that is not reflective of the inflow. This would result in an erroneously low $[CH_2O]_{OF\ extrap\ t=0}$ value that would in turn yield erroneously high CH_2O SEs. At present, we have no way of estimating the magnitude of this potential error, but this high SE should not be considered in the same group as the other determinations.

As previously discussed, the WRF-Chem modeling result for the 29 May storm only produces a SE result (53%) that is consistent with the other two approaches when an ice retention value of 0% ($r_f = 0$, complete degassing) is assumed. The sensitivity runs with ice retentions > 0 in all four cases produce unrealistically large CH_2O SEs of 97 to 99%. There are large uncertainties in ice retention factors for soluble gases like CH_2O, and this can make a large difference in estimating the effective transport of HO_x precursors in convection. Although the number of cases studied here are limited, and the observed specific ice hydrometer categories (pristine ice, snow, and graupel) are not known here, the results from the WRF-Chem simulations are highly suggestive that CH_2O has little or no retention in ice. We note, however, that the present WRF-Chem simulations do not include potential aqueous phase loss of CH_2O by OH in solution to produce formic acid. The potential influence of this mechanism clearly needs further investigation. Additional convection studies are also required to make more definitive statements regarding CH_2O and ice retention in different types of convection. To this end, we are presently analyzing our CH_2O measurements acquired during the 2013 SEAC⁴RS study over the southeast United States, and this will be the subject of a separate paper. During SEAC⁴RS, we intercepted numerous convective storm cores with approximately an order of magnitude lower vertical velocity at various altitudes. Such contrasting conditions will help in addressing the questions raised in this study.

6.2. CH_2O SE Comparisons With Other Studies and Results Using Other Mixing Models

It is also interesting to note the similar CH_2O SE values for storms where biogenic activity is high (29 May and 11 June) and where it is not (6 June). By contrast, *Borbon et al.* [2012] determined a very low CH_2O SE of 4% ± 1% for an MCS storm over a tropical forest region of Oueme with high biogenic activity. These authors speculated that potentially additional soluble oxygenated species of biogenic origin could effectively compete with aqueous CH_2O for the available OH in solution, thus reducing the effective CH_2O Henry's law value and hence the amount scavenged. Our results over contrasting source regions, although limited in number, do not show this behavior. *Borbon et al.* [2012] also reported CH_2O SE results for three other storms over other source regions of West Africa and determined SE values based on their three-component mixture model of: 26% ± 8%, 39% ± 12%, and 13% ± 4%.

The CH_2O SEs for the four case studies of *Borbon et al.* [2012] are all lower than the cases in the present study. In an effort to determine if such differences could be related to the methodology, we further examine here the 29 May storm results employing other mixing models using the same 29 May IF (4601 pptv) and OF (1093 pptv) values as the present study. This provides further insights into factors that might affect CH_2O SE determinations and in the process further highlights the fact that different mixing models require different tracer characteristics. We calculate here 29 May CH_2O SEs employing (1) the *Cohan et al.* [1999] two-

Table 8. Comparisons of CH_2O SE Determinations for the 29 May Storm Case Employing Different Approaches on the Same Data Set (CH_2O IF = 4601 pptv, and OF = 1093 pptv)[a]

Method	Tracers Employed	SE %
Alt. dep. entrainment, constant α	n,i-butane, n,i-pentane, n-hexane, and n-heptane tracers	54 ± 5
Alt. dep. entrainment, variable α from WRF		58
Butane ratio	n-butane	51 ± 5
WRF-Chem. simulation with $r_{f=0}$		53
Cohan et al. [1999][b]	n,i-butane and n,i-pentane	54 ± 4
	CO and ethane	69 ± 1
Borbon et al. [2012][c]	CO-n-butane and CH_4-i-butane	54
Yang et al. [2015][d]	CO, acetone, benzene, and ethane	57 ± 8

[a]See text for definition of terms.
[b]Two-component model.
[c]Third-component model.
[d]Four-component model.

component mixture model, (2) the three-component *Borbon et al.* [2012] model, and (3) a recently published four-level mixing model by *Yang et al.* [2015]. We hereafter refer to these as the Cohan, Borbon, and Yang models. These results are summarized in Table 8 along with our 29 May values. In these comparisons we employ factors (entrainment and dilution) deduced directly from the individual approaches.

In the Cohan model, the CH_2O SE is calculated from:

$$SE = 1 - \frac{\{Y_{conv} - (1 - \beta)Y_{UT}\}}{\beta Y_{BL}}. \tag{11}$$

The terms with their values in parenthesis Y_{conv} (1093 pptv), Y_{UT} (73 pptv), and Y_{BL} (4601 pptv) represent CH_2O in the convective OF, the upper tropospheric background, and the BL inflow, respectively. The β term, which represents the fraction of BL air present in fresh convective UT OF, is equivalent to our storm core deduced entrainment value α (7.6 ± 1%/km) averaged over the entire storm column (9.3 km), which yields a value of 0.71 ± 0.09. The β term is calculated from equation (12) employing six passive tracers (CO, ethane, n-butane, i-butane, n-pentane, and i-pentane):

$$X_{conv} = \beta X_{BL} + (1 - \beta)X_{UT}. \tag{12}$$

Here the terms X_{conv}, X_{BL}, and X_{UT} represent corresponding concentrations for the passive tracers in the convective OF, BL, and UT, respectively. Solving equation (12) results in $\beta = 0.58 \pm 0.13$, and this yields a CH_2O SE = 60 ± 8%. The 8% imprecision here only reflects the imprecision in the SE due to the imprecision in the β term. As shown in Figure 5, the butane and pentane tracers have the same vertical profile shape as CH_2O, and considering only these four tracers we calculate $\beta = 0.50 \pm 0.05$ and SE = 54 ± 4%. The latter value is identical with our combined average value of 54 ± 3%. Employing CO, which does not have the same altitude shape profile as CH_2O, and ethane, which is similar but does not go down to near zero values at midlatitudes yields $\beta = 0.74 \pm 0.03$ and SE = 69 ± 1%. It is interesting to note that if we employ the same six tracers above in our altitude-dependent mixing model, we determine an entrainment rate of 6.3 ± 2.0%/km (column entrainment rate = 6.3%/km × 9.3 km = 0.59) and a SE = 59 ± 8%. The Cohan model thus yields solutions for each tracer selected, and comparable values with the present study, when using the same tracers. This exercise also shows the sensitivity of our SE values on errors in our deduced entrainment rate: a change in the deduced entrainment rate of −1.3% produces a SE change of +5%. The SE imprecisions in Table 5 include this component along with additional imprecision terms in an error propagation analysis.

However, we believe that employing tracers with similar altitude profiles as CH_2O yields inherently more accurate results in the Cohan model and in our mixing model. The X_{UT} values for CO and ethane, 98 ppbv and 838 pptv, respectively, are nontrivial when compared to X_{conv} (CO = 123 ppb and ethane = 4070 pptv) and X_{BL} (CO = 133 ppbv and ethane = 5091 pptv), and these values and their uncertainties play a larger role in affecting the determination of β from equation (12) than n,i-butane and n,i-pentane. The corresponding X_{UT} values for n,i-butane and n,i-pentane are 32 pptv, 15 pptv, 8 pptv, and 8 pptv, respectively. These values are small compared to X_{conv} (779, 302, 213, and 198 pptv) and X_{BL} (1548, 513, 457, and 397 pptv) for the same tracers. Likewise, in our altitude-dependent entrainment model, the middle- and UT-tropospheric background cloud-free concentrations

for CO and ethane are still significant (in contrast to those for *n,i*-butane, *n,i*-pentane) and these values exert a significant influence on our deduced entrainment rates.

In the Borbon three-component mixture model, an additional term α was introduced to include the fraction of midlevel free tropospheric air (X_{FT}) entrained in the storm core, and equations (11) and (12) are appropriately modified to include this term (equations (13) and (14)). Solutions of α and β from this approach are obtained by solving a series of simultaneous equations involving the selected nonreactive tracers employing Borbon's equation (4):

$$X_{conv} = \beta X_{BL} + \alpha X_{FT} + (1 - \beta - \alpha)X_{UT}. \tag{13}$$

However, in contrast to the Cohan method, the solution of simultaneous equations generated from equation (13), requires nonreactive tracers with distinctly different vertical profiles; otherwise, the solutions may not converge. The same is also true for the four-level Yang mixing model, which will be discussed next. For example, using tracer pairs with similar vertical profiles *n,i*-butane, and CO-CH$_4$, to solve equations (13), our solutions do not converge. By contrast, if we solve these equations using pairs with different profiles (CO-*n*-butane, and CH$_4$-*i*-butane, as examples), we retrieve an average $\alpha = 0.47 \pm 0.11$ and $\beta = 0.47 \pm 0.04$, which when substituted into Borbon's SE equation using the same concentration values in connection with equation (11) above and a $Y_{FT} = 441$ pptv (median cloud-free 2–8 km CH$_2$O concentration):

$$SE = 1 - \frac{\{Y_{conv} - (1 - \beta - \alpha)Y_{UT}\}}{\beta\ Y_{BL} + \alpha\ Y_{FT}}, \tag{14}$$

yields a CH$_2$O SE = 54%, which again is in agreement with the other two methods previously discussed.

Yang et al. [2015] recently published a study for the same 29 May DC3 storm case studied in detail here employing a new 4-level mixing model to describe aerosol wet scavenging efficiencies. This study employed the four passive tracers CO, acetone, benzene, and ethane to determine the contribution to the anvil outflow from a well-mixed boundary layer (0–3 km), a buffer layer (3–7 km), a clean layer (7–9.5 km), and an UT outflow layer (9.5–12 km), with all layers here referring to pressure altitudes. A nonlinear least squares approach using finite difference derivatives was employed in solving a series of simultaneous equations, based on linear combinations of inflow and environmental background mixing ratios in the component layers, for processes involving lateral mixing, entrainment, detrainment, and convective updraft transport. We use the *Yang et al*. [2015] four-layer mixing model with their derived coefficients together with CH$_2$O mixing ratios determined here for the four component layers, to calculate [CH$_2$O]$_{Anvil\ core\ calc.}$ in Table 4a. Employing the 4601 pptv CH$_2$O IF value given in Table 4a and cloud-free median background CH$_2$O levels for the 3–7, 7–9.5, and 9.5 to 12 km layers, we deduce a value of [CH$_2$O]$_{Anvil\ core\ calc}$ = 2537 ± 446 pptv, which translates to a CH$_2$O SE = 57 ± 8% when using our extrapolated core value in equation (2). This value, which is remarkably similar to the 54% to 69% SE range obtained from the other three approaches, shows that although there is some sensitivity to the nonreactive tracers selected, four different mixing models, plus a butane ratio method, and a WRF-Chem simulation yield essentially the same CH$_2$O SE within the imprecision of the method in seven out of eight cases when employing the same IF and OF concentrations (see Table 8).

However, regardless of the approach employed, we again emphasize that it is extremely important to carefully select the BL inflow region that best represents the OF, and this is particularly critical for CH$_2$O where isoprene is a large source in many cases. As the isoprene levels vary significantly in the BL for the 29 May storm, simply averaging all the CH$_2$O values in the 0–3 km altitude range to represent IF (average CH$_2$O = 2504 ± 1216 pptv) will yield erroneous SE results. Employing this CH$_2$O value instead of the more representative IF value of 4601 ± 526 pptv would yield erroneously low CH$_2$O SEs of 20 ± 8% and 23 ± 13%, using respectively, our entrainment model and Yang's model. In addition, as the BL may also be heterogeneous with respect to our organic tracers (Table 6 shows large differences in *i-/n*-pentane ratios between inflow regions dominated by urban sources, oil and gas drilling sources, and fire sources, as an example), one has to be very careful in not blindly averaging all BL values in an effort to improve averaging statistics.

The results of this section, which are summarized in Table 8, thus suggest a range of CH$_2$O SE values from 51 to 69% are possible for the 29 May storm using different mixing models. Further, incorrectly employing an erroneous BL CH$_2$O mixing ratio based upon a large BL area average and not the true storm IF, could result in significantly reduced CH$_2$O SEs in the 20–23% range. Thus, in the 29 May storm case, proper selection of

corresponding IF and OF time segments is more important than the particular mixing model in the determination of CH_2O SEs.

7. Summary and Conclusions

In the present study we have developed and compared semi-independent methods for determining CH_2O scavenging efficiencies (SEs) for midlatitude convection over the central United States during the 2012 DC3 Study. The results of the present study were based upon measurements of CH_2O and other trace gases onboard the NASA DC-8 and the NSF/NCAR Gulfstream V (GV) aircraft, which sampled inflow and outflow in close coordination. In all cases, pertinent measurements used in this study from the two aircraft were compared by regression analysis, and where appropriate, corrections were applied to ensure that differences did not affect the results. In addition to measurements of CH_2O, this study relied heavily on the nonreactive and nonsoluble organic tracers i-/n-butane and i-/n-pentane (n-hexane and n-heptane in one case) in determining lateral entrainment values during convection as well as their ratios to ensure that inflow and outflow air masses did not have vastly different origins. This study also relied on ground-based radars and the resultant images to identify coherently related storm inflow and outflow time periods. Because in most cases the aircraft did not sample at the top of the storm cores, we developed an approach to extrapolate back to the storm core to account for the effects from dilution/mixing and possibility of chemical transformations in the anvil. This was accomplished by examining the outflow in each case employing aircraft positions superimposed on storm radar images, aircraft wind speeds, and directions along the flight tracks, to graphically estimate the time between aircraft sampling and the closest intense storm core. We eliminated stratospherically influenced air and only considered in this analysis outflow from comparable storm cores with radar reflectivities ≥ 40 dBZ. This allowed us to determine a single CH_2O outflow-mixing ratio extrapolated to time 0 emanating from the storm core.

The CH_2O scavenging efficiencies determined are remarkably consistent for the three strong convective cases (29 May, 6 June, and 11 June), both between storms and between the various approaches. The CH_2O scavenging efficiency ranges between 48% (47% if one employs the expanded IF region for 29 May) and 67%, and in all but one case, the various approaches are in agreement within the stated 1σ estimated precisions. The 22 June storm, which may be somewhat influenced by the High Park fire plume, resulted in a lower CH_2O SE of 41%. At this point we cannot rule out the influence of the fire plume on these results. WRF-Chem simulations of the 29 May storm produced agreement with the two measurement approaches only when the CH_2O ice retention factor was set to 0, suggesting complete or near-complete CH_2O degassing from ice. More comprehensive modeling studies involving potential aqueous phase loss of CH_2O by OH in solution to produce formic acid are required to further support this conclusion.

The combined average of the four CH_2O SE determinations for 29 May is $54 \pm 3\%$ ($n = 4$). The corresponding combined average for 6 June is $54 \pm 6\%$ ($n = 4$), for 11 June is $58\% \pm 13\%$ ($n = 2$), and 22 June is $41 \pm 4\%$ ($n = 2$), with the imprecision limits reflecting the standard deviation of the combined mean and not the individual imprecisions. This consistency in CH_2O SE is somewhat surprising given that these storms span a large geographic region of the United States (northeast Colorado, central Oklahoma, southern Missouri, northern Alabama, Mississippi, and Arkansas) with vastly different boundary layer compositions and involve differences in measured ice water content between storms. Moreover, the similar CH_2O SEs for storms where biogenic activity is high (29 May and 11 June) and where it is not (6 June), although limited in number, does not show the same type of behavior reported by *Borbon et al.* [2012]. That study postulated that potentially additional soluble oxygenated species of biogenic origin could effectively compete with aqueous CH_2O for the available OH in solution, thus reducing the effective CH_2O Henry's law value and hence the amount scavenged. Undoubtedly, additional storms over contrasting regions are needed to further study this aspect.

Moreover, additional studies are needed on a broader variety of storms over even larger geographic regions of the United States with larger differences in vertical velocity and liquid water content to further understand the scavenging CH_2O efficiency dependence on these parameters. The weaker convection on 21 May could provide added information in this regard. Unfortunately, the resulting high apparent SE for this day (81%) is compromised by the incoherence between inflow and outflow and the results, and therefore, the results are not reliable. This highlights the importance of firmly establishing the coherence between inflow and outflow to

obtain believable SE results. Additional studies, where different water hydrometeor phases are encountered, would be important to further support our present speculation that CH_2O is completely or nearly completely degassed from ice.

Further analysis investigating the 29 May storm employing the same IF and OF data employing three other mixing models, Cohan's two-component, Borbon's three-component, and Yang's four-component, resulted in the remarkably similar CH_2O SEs of 54% to 69%, further suggesting that differences with past studies are not caused by the mixing models and associated tracers employed. Further analysis on the 29 May storm indicated that proper selection of corresponding IF and OF time segments is more important than the particular mixing model employed. Incorrectly employing an erroneous BL CH_2O mixing ratio based upon a large BL area average and not the true storm IF could result in significantly reduced CH_2O SEs in the 20–23% range. Although this issue remains a possibility to explain CH_2O SE differences with past studies, unfortunately we have no way to unequivocally disentangle this effect from those due to differences in storm dynamics and microphysics. Continued studies on a wide variety of storms should be carried out to further examine the effects of storm dynamics and microphysics on CH_2O SEs.

The results of this study are in contrast to the more aged and weaker convective cases studied by *Fried et al.* [2008b], where photochemical production of CH_2O from its convectively transported precursors was found to be more important than direct convective transport of CH_2O from the boundary layer. In contrast to the strong convective cases studied here, the convective outflow studied by *Fried et al.* [2008b] was typically more than several hours old. For the strong convective cases studied here, the ratio of the measured outflow CH_2O concentrations when extrapolated to the storm cores (575 to 1524 pptv) to the inflow values ranged between ~ 24 to 50%. The CH_2O SE results of the present study is an important first step for improving our understanding of HO_x production downwind of convection, which is crucial for estimating O_3 production in the upper troposphere.

References

Ancellet, G., J. Leclair de Bellevue, C. Mari, P. Nedelec, A. Kukui, A. Borbon, and P. Perros (2009), Effects of regional-scale and convective transports on tropospheric ozone chemistry revealed by aircraft observations during the wet season of the AMMA campaign, *Atmos. Chem. Phys.*, 9, 383–411.

Apel, E. C., et al. (2014), Upper tropospheric ozone production from lightning NO_x-impacted convection; smoke ingested case study from the DC3 campaign, *J. Geophys. Res. Atmos.*, 120, 2505–2523, doi:10.1002/2014JD022121.

Arakawa, A., and W. H. Schubert (1974), Interaction of a cumulus cloud ensemble with the large-scale environment, part i, *J. Atmos. Sci.*, 31, 674–701.

Avery, M., et al. (2010), Convective distribution of tropospheric ozone and tracers in the Central American ITCZ region: Evidence from observations during TC4, *J. Geophys. Res.*, 115, D00J21, doi:10.1029/2009JD013450.

Barret, B., et al. (2010), Impact of West African Monsoon convective transport and lightning NO_x production upon the upper tropospheric composition: A multi-model study, *Atmos. Chem. Phys.*, 10, 5719–5738, doi:10.5194/acp-10-5719-2010.

Barth, M. C., S.-W. Kim, W. C. Skamarock, A. L. Stuart, K. E. Pickering, and L. E. Ott (2007), Simulations of the redistribution of formaldehyde, formic acid, and peroxides in the 10 July 1996 stratospheric-tropospheric experiment: Radiation, aerosols, and ozone deep convection storm, *J. Geophys. Res.*, 112, D13310, doi:10.1029/2006JD008046.

Barth, M. C., J. Lee, A. Hodzic, G. Pfister, W. C. Skamarock, J. Worden, J. Wong, and D. Noone (2012), Thunderstorms and upper troposphere chemistry during the early stages of the 2006 North American Monsoon, *Atmos. Chem. Phys.*, 12, 11,003–11,026, doi:10.5194/acp-12-11003-2012.

Barth, M. C., J. Crounse, J. St. Clair, and P. Wennberg (2015), The Deep Convective Clouds and Chemistry (DC3) field campaign, *Bull. Am. Meteorol. Soc.*, 96(8), 1281–1309, doi:10.1175/BAMS-D-13-00290.1.

Barth, M. C., et al. (2016), Convective transport and scavenging of peroxides by thunderstorms observed over the Central U.S. during DC3, *J. Geophys. Res. Atmos.*, doi:10.1002/2015JD024570.

Bela, M. M., et al. (2016), Wet scavenging of soluble gases in DC3 deep convective storms using WRF-Chem simulations and aircraft observations, *J. Geophys. Res. Atmos.*, doi:10.1002/2015JD024623.

Bertram, T. H., et al. (2007), Direct measurements of the convective recycling of the upper troposphere, *Science*, 315, 816–820.

Biggerstaff, M. I., L. J. Wicker, J. Guynes, C. Ziegler, J. M. Straka, E. N. Rasmussen, A. Doggett, L. D. Carey, J. L. Schroeder, and C. Weiss (2005), The shared mobile atmospheric research and teaching radar: A collaboration to enhance research and teaching, *Bull. Am. Meteorol. Soc.*, 86, 1263–1274, doi:10.1175/BAMS-86-9-1263.

Blake, N. J., et al. (2015), Spatial distributions and source characterization of trace organic gases during SEAC[4]RS and comparison to DC3 Abstract A33C-3197 presented at 2015 Fall Meeting, AGU, San Francisco, Calif., Dec.

Borbon, A., et al. (2012), Transport and chemistry of formaldehyde by mesoscale convective systems in West Africa during AMMA 2006, *J. Geophys. Res.*, 117, D12301, doi:10.1029/2011JD017121.

Brunner, D., J. Staehelin, and D. Jeker (1998), Large-scale nitrogen oxide plumes in the tropopause region and implications for ozone, *Science*, 282, 1305–1309.

Burgess, D. W., E. R. Mansell, C. M. Schwarz, and B. J. Allen (2010), Tornado and tornadogenesis events seen by the NOXP, X-band, dual-polarization radar during VORTEX2 2010, Preprints, 25th Conf. on Severe Local Storms, Denver, CO, Amer. Meteor. Soc., 5.2. [Available at https://ams.confex.com/ams/25SLS/techprogram/paper_176164.htm.]

Calvert, J. G., R. G. Derwent, J. J. Orlando, G. S. Tyndall, and T. J. Wallington (2008), *Mechanisms of Atmospheric Oxidation of the Alkanes*, Oxford Press, New York.

Carbone, R. E., J. D. Tuttle, D. A. Ahijevych, and S. B. Trier (2002), Inferences of predictability associated with warm season precipitation episodes, *J. Atmos. Sci.*, *59*, 2033–2056.

Chatfield, R. B., and P. J. Crutzen (1984), Sulfur dioxide in remote ocean air: Cloud transports of reactive precursors, *J. Geophys. Res.*, *89*, 7111–7132, doi:10.1029/JD089iD05p07111.

Chin, M., P. Ginoux, S. Kinne, B. N. Holben, B. N. Duncan, R. V. Martin, J. A. Logan, A. Higurashi, and T. Nakajima (2002), Tropospheric aerosol optical thickness from the GOCART model and comparisons with satellite and sunphotometer measurements, *J. Atmos. Sci.*, *59*, 461–483.

Cohan, D. S., M. G. Schultz, D. J. Jacob, B. G. Heikes, and D. R. Blake (1999), Convective injection and photochemical decay of peroxides in the tropical upper troposphere: Methyl iodide as a tracer of marine convection, *J. Geophys. Res.*, *104*(D5), 5717–5724, doi:10.1029/98JD01963.

Colomb, A., et al. (2006), Airborne measurements of trace organic species in the upper troposphere over Europe: The impact of deep convection, *Environ. Chem.*, *3*(4), 244–259, doi:10.1071/EN06020.

Cooper, O. R., et al. (2006), Large upper tropospheric ozone enhancements above mid-latitude North America during summer: In situ evidence from the IONS and MOZAIC ozone monitoring network, *J. Geophys. Res.*, *111*, D24S05, doi:10.1029/2006JD007306.

Cotton, W. R., G. D. Alexander, R. Hertenstein, R. L. Walko, R. L. McAnelly, and M. Nicholls (1995), Cloud venting—A review and some new global annual estimates, *Earth Sci. Rev.*, *39*(3-4), 169–206.

Crawford, J. H., et al. (2000), Evolution and chemical consequences of lightning-produced NO_x observed in the North Atlantic upper troposphere, *J. Geophys. Res.*, *105*, 19,795–19,809, doi:10.1029/2000JD900183.

Crounse, J. D., et al. (2009), Biomass burning and urban air pollution over the Central Mexican Plateau, *Atmos. Chem. Phys.*, *9*, 4929–4944, doi:10.5194/acp-9-4929-2009.

DeCaria, A. J., K. E. Pickering, G. L. Stenchikov, and L. E. Ott (2005), Lightning-generated NO_x and its impact on tropospheric ozone production: A three-dimensional modeling study of a Stratosphere-Troposphere Experiment: Radiation, Aerosols and Ozone (STERAO-A) thunderstorm, *J. Geophys. Res.*, *110*, D14303, doi:10.1029/2004JD005556.

Dickerson, R. R., et al. (1987), Thunderstorms: An important mechanism in the transport of air pollutants, *Science*, *235*, 460–465.

Dye, J. E., et al. (2000), An overview of the Stratosphere-Troposphere Experiment: Radiation, Aerosols, and Ozone (STERAO)-Deep Convection experiment with results for the July 10, 1996 storm, *J. Geophys. Res.*, *105*, 10,023–10,045, doi:10.1029/1999JD901116.

Easter, R. C., and J. M. Hales (1983), Interpretations of the OSCAR data for reactive gas scavenging, in *Precipitation Scavenging, Dry Deposition, and Resuspension*, edited by H. R. Pruppacher, R. G. Semonin, and W. G. N. Slinn, pp. 649–662, Elsevier Sci., New York.

Emmons, L. K., et al. (2010), Description and evaluation of the Model for Ozone and Related chemical Tracers, version 4 (MOZART-4), *Geosci. Model Dev.*, *3*, 43–67, doi:10.5194/gmd-3-43-2010.

Fierro, A. O., E. R. Mansell, C. Ziegler, and D. R. MacGorman (2012), Application of a lightning data assimilation technique in the WRF-ARW model at cloud-resolving scales for the Tornado Outbreak of 24 May 2011, *Mon. Weather Rev.*, *140*, 2609–2627.

Fried, A., et al. (2008a), Formaldehyde over North America and the North Atlantic during the summer 2004 INTEX campaign: Methods, observed distributions, and measurement-model comparisons, *J. Geophys. Res.*, *113*, D10302, doi:10.1029/2007JD009185.

Fried, A., et al. (2008b), Role of convection in redistributing formaldehyde to the upper troposphere over North America and the North Atlantic during the summer 2004 INTEX campaign, *J. Geophys. Res.*, *113*, D17306, doi:10.1029/2007JD009760.

Giorgi, F., and W. L. Chameides (1986), Rainout lifetimes of highly soluble aerosols and gases as inferred from simulations with a general circulation model, *J. Geophys. Res.*, *91*, 14,367–14,376, doi:10.1029/JD091iD13p14367.

Grell, G. A., S. E. Peckham, R. Schmitz, S. A. McKeen, G. Frost, W. C. Skamarock, and B. Eder (2005), Fully coupled online chemistry within the WRF model, *Atmos. Environ.*, *39*, 6957–6975.

Guenther, A., T. Karl, P. Harley, C. Wiedinmyer, P. I. Palmer, and C. Geron (2006), Estimates of global terrestrial isoprene emissions using MEGAN (Model of Emissions of Gases and Aerosols from Nature), *Atmos. Chem. Phys.*, *6*, 3181–3210.

Houze, R. A. (1993), *Cloud Dynamics*, Academic Press, San Diego.

Houze, R. A., Jr., M. I. Biggerstaff, S. A. Rutledge, and B. F. Smull (1989), 1989: Interpretation of Doppler weather radar displays of midlatitude mesoscale convective systems, *Bull. Am. Meteorol. Soc.*, *70*, 608–619, doi:10.1175/1520-0477(1989)070<0608:IODWRD>2.0.CO;2.

Huntrieser, H., et al. (2002), Airborne measurements of NO_x, tracer species, and small particles during the European Lightning Nitrogen Oxides Experiment, *J. Geophys. Res.*, *107*(D11), 4113, doi:10.1029/2000JD000209.

Jaeglé, L., et al. (1997), Observed OH and HO_2 in the upper troposphere suggest a major source from convective injection of peroxides, *Geophys. Res. Lett.*, *24*(24), 3181–3184, doi:10.1029/97GL03004.

Jaeglé, L., D. J. Jacob, W. H. Brune, D. Tan, I. C. Faloona, A. J. Weinheimer, B. A. Ridley, T. L. Campos, and G. W. Sachse (1998), Sources of HO_x and production of ozone in the upper troposphere over the United States, *Geophys. Res. Lett.*, *25*(10), 1709–1712, doi:10.1029/98GL00041.

Kormann, R., et al. (2003), Formaldehyde over the eastern Mediterranean during MINOS: Comparison of airborne in-situ measurements with 3D- model results, *Atmos. Chem. Phys.*, *3*, 851–861, doi:10.5194/acp-3-851-2003.

Lelieveld, J., et al. (2002), Global air pollution crossroads over the Mediterranean, *Science*, *298*(5594), 794–799, doi:10.1126/science.1075457.

Leriche, M., J.-P. Pinty, C. Mari, and D. Gazen (2013), A cloud chemistry module for the 3-D cloud-resolving mesoscale model Meso-NH with application to idealized cases, *Geosci. Model Dev.*, *6*, 1275–1298, doi:10.5194/gmd-6-1275-2013.

Luo, Z. J., G. Y. Liu, and G. L. Stephens (2010), Use of A-Train data to estimate convective buoyancy and entrainment rate, *Geophys. Res. Lett.*, *37*, L09804, doi:10.1029/2010GL042904.

Mari, C., et al. (2003), On the relative role of convection, chemistry, and transport over the South Pacific Convergence Zone during PEM-Tropics B: A case study, *J. Geophys. Res.*, *107*(D2), 8232, doi:10.1029/2001JD001466.

Müller, J.-F., and G. Brasseur (1999), Sources of upper tropospheric HO_x: A 3-dimensional study, *J. Geophys. Res.*, *104*(D1), 1705–1715, doi:10.1029/1998JD100005.

Neu, J. L., and M. J. Prather (2012), Toward a more physical representation of precipitation scavenging in global chemistry models: Cloud overlap and ice physics and their impact on tropospheric ozone, *Atmos. Chem. Phys.*, *12*, 3289–3310.

Pickering, K. E., A. M. Thompson, R. R. Dickerson, W. T. Luke, D. P. McNamara, J. P. Greenberg, and P. R. Zimmerman (1990), Model calculations of tropospheric ozone production potential following observed convective events, *J. Geophys. Res.*, *95*, 14,049–14,062, doi:10.1029/JD095iD09p14049.

Pickering, K. E., et al. (2001), Trace gas transport and scavenging in PEM-Tropics B South Pacific Convergence Zone convection, *J. Geophys. Res.*, *106*(D23), 32,591–32,602, doi:10.1029/2001JD000328.

Raper, J. L., M. M. Kleb, D. J. Jacob, D. D. Davis, R. E. Newell, H. E. Fuelberg, R. J. Bendura, J. M. Hoell, and R. J. McNeal (2001), Pacific exploratory mission in the tropical Pacific: PEM-Tropics B, March–April 1999, *J. Geophys. Res.*, *106*(D23), 32,401–32,425, doi:10.1029/2000JD900833.

Richter, D., P. Weibring, J. Walega, A. Fried, S. M. Spuler, and M. S. Taubman (2015), Compact highly sensitive multi-species airborne mid-IR spectrometer, *Appl. Phys. B*, doi:10.1007/s00340-015-6038-8.

Ridley, B., et al. (2004a), Convective transport of reactive constituents to the tropical and mid-latitude tropopause region: I. Observations, *Atmos. Environ.*, *38*, 1259–1274.

Ridley, B., et al. (2004b), Florida thunderstorms: A faucet of reactive nitrogen to the upper troposphere, *J. Geophys. Res.*, *109*, D17305, doi:10.1029/2004JD004769.

Sander, R. (2015), Compilation of Henry's law constants (version 4.0) for water as solvent, *Atmos. Chem. Phys.*, *15*, 4399–4981, doi:10.5194/acp-15-4399-2015.

Sander, S. P., et al. (2011), Chemical kinetics and photochemical data for use in atmospheric studies: Evaluation number 17 JPL Publ., 10-6, 34 pp.

Stickler, A., H. Fischer, J. Williams, M. de Reus, R. Sander, M. G. Lawrence, J. N. Crowley, and J. Lelieveld (2006), Influence of summertime deep convection on formaldehyde in the middle and upper troposphere over Europe, *J. Geophys. Res.*, *111*, D14308, doi:10.1029/2005JD007001.

Tabazadeh, A., R. J. Yokelson, H. B. Singh, P. V. Hobbs, J. H. Crawford, and L. T. Iraci (2004), Heterogeneous chemistry involving methanol in tropospheric clouds, *Geophys. Res. Lett.*, *31*, L06114, doi:10.1029/2003GL018775.

Voisin, D., M. Legrand, and N. Chaumerliac (2000), Scavenging of acidic gases (HCOOH, CH_3COOH, HNO_3, HCl, and SO_2) and ammonia in mixed liquid-solid water clouds at the Puy de Dôme mountain (France), *J. Geophys. Res.*, *105*, 6817–6835, doi:10.1029/1999JD900983.

Weibring, P., D. Richter, A. Fried, J. Walega, and C. Dyroff (2006), Ultra-high precision mid-IR spectrometer II: System description and spectroscopic performance, *Appl. Phys. B*, *85*, 207–218, doi:10.1007/s00340-006-2300-4.

Weibring, P., D. Richter, J. G. Walega, and A. Fried (2007), First demonstration of a high performance difference frequency spectrometer on airborne platforms, *Opt. Express*, *15*(21), 13,476–13,495.

Wennberg, P. O., et al. (1998), Hydrogen radicals, nitrogen radicals, and the production of O_3 in the upper troposphere, *Science*, *279*, 49–53.

Wiedinmyer, C., S. K. Akagi, R. J. Yokelson, L. K. Emmons, J. A. Al-Saadi, J. J. Orlando, and A. J. Soja (2011), The Fire Inventory from NCAR (FINN): A high resolution global model to estimate the emissions from open burning, *Geosci. Model Dev.*, *4*, 625–641, doi:10.5194/gmd-4-625-2011. [Available at http://scholarworks.umt.edu/chem_pubs/8.]

Yang, Q., et al. (2015), Aerosol transport and wet scavenging in deep convective clouds: A case study and model evaluation using a multiple passive tracer analysis approach, *J. Geophys. Res. Atmos.*, *120*, 8448–8468, doi:10.1002/2015JD023647.